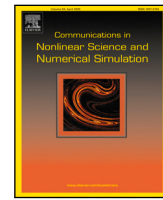




Contents lists available at ScienceDirect

Communications in Nonlinear Science and Numerical Simulation

journal homepage: www.elsevier.com/locate/cnsns

Research paper



Triply periodic minimal surfaces based topology optimization for the hydrodynamic and convective heat transfer

Qing Xia ^a, Junxia Zhu ^a, Qian Yu ^b, Junseok Kim ^c, Yibao Li ^{a,*}^a School of Mathematics and Statistics, Xi'an Jiaotong University, Xi'an 710049, PR China^b School of Mathematical Sciences, Peking University, Beijing 100871, PR China^c Department of Mathematics, Korea University, Seoul 02841, Republic of Korea

ARTICLE INFO

Keywords:

Triply periodic minimal surface
Heat sinks
Shape and performance control
Phase-field modeling
Unconditionally energy stability

ABSTRACT

Triply periodic minimal surfaces (TPMS), possessing diverse and crucial properties for thermal convection analysis, hold significant promise for topology optimization in convective and hydrodynamic systems. This study aims to develop an innovative topology optimization method based on TPMS for channel shape design. We focus on maximizing heat dissipation and mass flux while maintaining a constant mean curvature. The channel structures undergo free evolution during the optimization process, resulting in efficient and intricate geometries based on the TPMS assumption. To incorporate TPMS properties, we modify the original energy formulation, which comprises kinetic energy, thermal energy, and Ginzburg–Landau energy. The governing system encompasses the phase field model, the Darcy–Stokes model, and the reaction–diffusion heat transfer model. The hydrodynamic response within the phase change structure is computed by solving the transient Darcy–Stokes equation augmented with a temperature-dependent diffusion term. To achieve second-order temporal and spatial accuracy, we employ the Crank–Nicolson method for the time scale and the central difference method for the spatial scale. Through the utilization of the Lagrange multiplier method, we establish the unconditional decrease of the discretized original energy. This implies that the proposed scheme can utilize a large time step. To verify the robustness of our proposed method, we conduct several numerical tests from both qualitative and quantitative perspectives. The results demonstrate the effectiveness of our method in enhancing heat and mass transfer capabilities.

1. Introduction

Determining the impacts of the channel shape on heat transfer plays a significant role in designing and optimizing the channel structure of heat sinks [1,2]. The topology optimization method can utilize the characteristics of heat transfer [3], external load [4,5], shape change [6,7] and fluids flow [8], to design the shapes of the channel to maximize heat dissipation, improve the fluid flux and reduce the pressure drop [9,10]. In light of the rapid development of topology optimization technology, it is extremely hard to ignore the idea of designing heat exchanger by optimized-based method [11,12]. Wu et al. [13] developed an optimization model for the thermal flow channels with porous structures in the radial direction, which increases the contact surface area and enhances the capacity of heat transfer. In order to minimize the thermal resistance in integrated systems and maximize the thermal protection of cooling areas, Soprani et al. [14] proposed a topology optimization approach for integration of thermoelectric modules with

* Corresponding author.

E-mail address: yibaoli@xjtu.edu.cn (Y. Li).

URL: <http://gr.xjtu.edu.cn/web/yibaoli> (Y. Li).

specific design constraint. Høghøj et al. [15] proposed a density-based method for the topology optimization of heat exchangers with binary fluids, which aims to maximize the thermal conduction under the constraint of the maximum pressure drop. The erosion-dilation based identification method has been applied to generate the solid interface with a minimum wall thickness. The Brinkman penalty technique [16] has been performed to ensure negligible velocity outside of the fluid domains. The optimized results outperform the baseline design in terms of heat transfer performance, indicating that the topology optimization method works well for thermal conduction. Pizzolato et al. [17] coupled large design freedom to the corresponding physics modeling and developed a design approach for heat transfer intensification by using topology optimization combined with multi-phase computational fluid dynamics [18]. Their results indicate that fluid flow is crucial for heat performance under the impacts of topology optimization.

There are two basic categories currently being adopted in the field of multiscale optimization, i.e., microstructure design [19] and macrostructure design [20]. The former is to find the structural topology which renders a given design objective an optimum value while the latter is performed in conjunction with a shape optimization under the global constraints [21]. The two-scale concurrent design provides higher frequency responses compared to those obtained from single-scale topology optimizations [22]. However, it is a crucial and tough task for the common technique to deal with the connectivity within the topology optimization framework [10], which are limited by the shape of microstructures. The triply periodic minimal surface structures, which are periodic in three directions and of constant mean curvature for all points on the surfaces, have been attracting considerable interest as the cellular structures for the microstructure-based topology optimization of thermal fluids due to the favorable surface continuity [23,24], good mechanical performance [25,26], symmetry and structural stability [3], and large specific surface area [27]. The common TPMS structures can be described as Primitive surface, Diamond surface, Gyroid surface, and I-WP surface, which are precisely controlled by implicit functions [28]. Li et al. [29] utilized the TPMS structure to propose two novel heat exchangers for the supercritical carbon dioxide based Brayton cycle. Compared to the efficiency of the conventional Rankine cycles, the TPMS-based heat exchangers can greatly improve overall thermal performance. Iyer et al. [30] characterized the flow and heat transfer properties of the TPMS based structures by computing the friction factors with the laminar flow regime. Their work provided the heuristic suggestions on optimizing the heat transfer performance and pressure drop characteristics for subsequent TPMS based studies. Cheng et al. [31] developed a TPMS-based method to customize the morphology of porous media with controlled pore features. The morphological analysis were performed to connect the performance features of the TPMS structure and the geometric parameters, which can provide heuristic suggestions on quantitative index for further investigating the topology optimization of heat exchanger [32]. The existing state-of-the-art studies [33–35] demonstrated that the porous structure of TPMS works well for the heat and mass transfer with high strength performance and lower flow resistance by comparing with the simple cubic stacking structure. The topological optimization of channel form based on TPMS structure is in its early stages, with the primary goal of researching infrastructure characteristics.

Few studies have been conducted to consider the possible effects of thermal fluid topology optimization based on the TPMS structures to further improve the physical performance. Wang et al. [36] proposed an efficient representation and optimization for heat dissipation based on TPMS porous structures. They derived a novel representation by inheriting the good properties of TPMS and formulated the mean temperature distribution with the given constraints to maximize the heat dissipation. However, the optimization process did not take into account the impacts of fluid flow, which is significant for heat transfer and conduction. Modrek et al. [37] proposed a multi-objective topology optimization system based on the solid isotropic penalty method, which optimized both the thermal and structural objective function to obtain an optimized structure with better heat dissipation performance and enhanced structural integrity. Although the optimized structures had better thermal conductivity, there was no discussion on the influence of structural difference on heat transfer and rigidity. Al-Ketan et al. [38] developed three dimensional computational fluid dynamic model for the uniform heat sinks and topologically graded heat sinks based on the TPMS structures to compare their corresponding capability in convection domains. This work is one of the first investigation to consider the influence of the TPMS lattices differences. Although only the gradient porosity is involved, it provides a novel direction for the topology optimization of heat flow based on TPMS structure since the morphology of the porous structures has significant impact on the heat and mass transfer. Meanwhile, considering the variations in physical properties inherent to different microscopic lattices with distinct topologies, establishing diverse assembly methods to integrate a multitude of features is deemed an appropriate approach [39]. The proposition of newly conceived lattice structures is substantiated by the proliferation of additive manufacturing methodologies, including but not limited to 3D printing.

The objective of this paper is to explore thermal fluid topology optimization using TPMS structures, aiming to minimize the objective function under constraints such as maximizing heat dissipation, maintaining a constant mean curvature, and maximizing fluid flux. By leveraging the TPMS-based assumption, the channel structures undergo free evolution during the optimization process, leading to the creation of more efficient and intricate geometries. By incorporating the constant curvature property of TPMS structures into the modified Ginzburg–Landau energy [40], a novel objective functional is obtained. This functional can be minimized while considering the thermal-hydrodynamic constraints of the phase-change system. The phase-field-based optimization system is proven to be unconditionally energy stable. The hydrodynamic response within the phase-change structures is determined by solving the thermal system, which consists of the transient Darcy–Stokes equation and the reaction–diffusion heat transfer equation. For the discretization of the governing system, the Crank–Nicolson (CN) method [41] is employed to achieve second-order temporal accuracy, while the central difference method is utilized to attain second-order spatial accuracy. To ensure stability and mitigate the influence of higher-order nonlinear terms on the proposed scheme, the Lagrangian multiplier method is applied to the discrete system. The discrete system is proven to be unconditionally energy stable, indicating that large time steps can be utilized for computation. To demonstrate the robustness of our method, numerous numerical tests will be conducted from both qualitative and quantitative perspectives. The primary contributions of this paper can be summarized as follows: (i) The formulation of the topology optimization model for thermal fluids facilitates the maximization of heat dissipation and structural connectivity, while

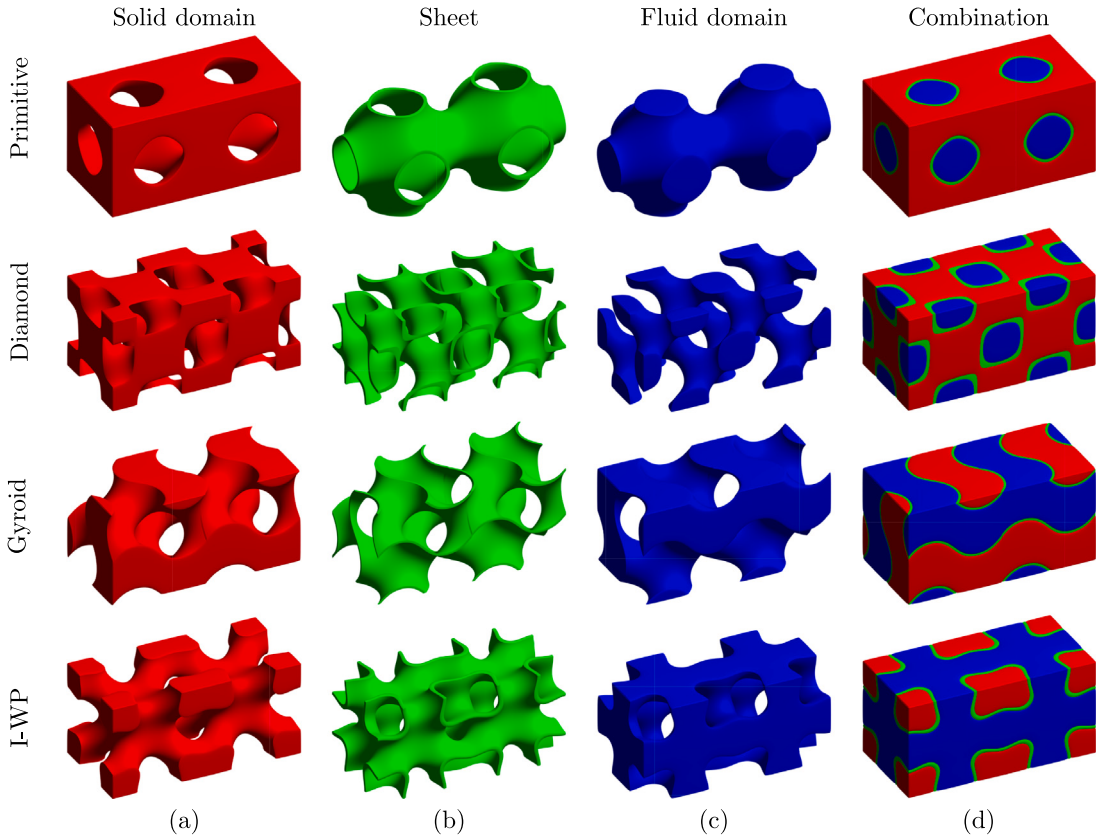


Fig. 1. Schematic demonstration of four types TPMS structures. From the top row to the bottom row, the results are from the Primitive, Diamond, Gyroid, and I-WP structures, respectively. (a) Solid domain. (b) Sheet structure. (c) Fluid domain. (d) Combination of the three domain.

simultaneously ensuring a consistent curvature along the channel. (ii) The proposed optimization method operates within a universal framework, not limited by physical properties such as TPMS structure types, sizes, and porosities. Improved performance can be achieved through the modified fluid channel, which preserves the key geometric features of the original TPMS structure. (iii) The transformation of the subregional optimization problem into a global optimization problem, reducing the computational burden associated with solving partial differential equations.

The outline of this paper is as follows: In Section 2, we take the variational derivation from the energy cost function and establish the phase field based model for the convective heat transfer process to achieve the topology optimization of composite structures. In Section 3, we discretize the governing equations and prove rigorously the unconditional discrete energy stability of the proposed system. Furthermore, we provide the numerical solutions of the governing equations. Various quantitative and qualitative numerical tests have been performed in Section 4. In summary, conclusive remarks have been drawn in Section 5.

2. Methodology

In this section, we briefly review the hydrodynamic topology optimization model under the guidance of the phase field constraints. After the introduction of the energy cost functional, we obtain the governing equations by the variational derivation, whose solutions convert the target functional decrease to its minimum value. Furthermore, the energy dissipation law will be unconditionally preserved by the established system.

2.1. Phase field model based on the gradient variation of energy

We first introduce the original optimization problem by minimizing a certain objective functional with the constraints of incompressible Darcy–Stokes equation and reaction–diffusion heat transfer equation. Assume the computation domain is a given Lipschitz domain $\Omega \subseteq \mathbb{R}^m (m = 2, 3)$. Let $\partial\Omega$ denote its boundary and the outer normal vector for Ω is denoted by \mathbf{n} . Let us introduce ϕ as a characteristic function of bounded variation in Ω and denote $V(\Omega, \{0, 1\})$ as the space of functions of bounded variation in Ω , which can be interpreted as $\phi = 1 (\mathbf{x} \in \Omega_f)$ and $\phi = 0 (\mathbf{x} \in \Omega_s)$. By introducing the Caccioppoli set $E \subset \Omega$ with

$\phi := \chi_E \in V(\Omega, \{0, 1\})$, we can use the corresponding Caccioppoli set $\Omega_f := \{\phi = 1\}$ to define the fluid subdomain. Furthermore, we denote the solid subdomain as $\Omega_s = \Omega \setminus \Omega_f$. We define the inner product (\cdot, \cdot) and norm $\|\cdot\|$ for matrix functions as follows:

$$(\mathbf{F}, \mathbf{G}) = \sum_{m,n} \int_{\Omega} \mathbf{F}_{m,n} \mathbf{G}_{m,n} d\mathbf{x}, \quad \|\mathbf{F}\| = (\mathbf{F}, \mathbf{F})^{1/2}, \quad (1)$$

where \mathbf{F} and \mathbf{G} are matrix functions defined in Ω . Then inner products of scalar and vector functions can be analogously defined. Before establishing the topology optimization model for thermal fluids, we first introduce the region division considering the TPMS-based channel, whose schematic demonstration has been shown in Fig. 1. As can be seen from the figure, the whole domain can be divided into three parts, the solid domain, the fluid domain and the sheet structure with a certain thickness. It should be pointed out that the material properties of solid domain and sheet structure may be different in real physical context. In this paper, we simplify the computation by assuming that the sheet structure has the same properties as the solid domain and only consider the topology optimization on the fluid domain. Considering the general absence of minimizers in optimization problems within this context [42], we incorporate a perimeter regularization. The original topology optimization problem can be defined as the minimization of the following objective functional:

$$\min_{\Omega} \mathcal{J}_{\text{ori}}(\mathbf{u}, T) = \int_{\Omega_f} \left(\frac{\eta}{2} |\nabla \mathbf{u}|^2 - \mathbf{u} \cdot \mathbf{f} \right) d\mathbf{x} + \int_{\Omega} \frac{K}{2} |T|^2 d\mathbf{x} + \gamma \Gamma(\Omega_f), \quad (2)$$

where η is the viscosity of the fluid, \mathbf{f} is the external force, $\nabla \mathbf{u}$ is the gradient of the fluid velocity \mathbf{u} , Γ is the length of the perimeter of Ω_f , K is the thermal conductivity coefficient, and γ is the positive penalized parameter. While the optimization problem in shape and topology yields a broad spectrum of potential solutions, numerical methods and analytical approaches tend to favor increased regularity when addressing optimization challenges. In this paper, we employ a fictitious material approach [43], wherein the void region is replaced with a very weak material. The region outside the fluid is substituted with a porous medium. Specifically, by replacing the whole computational domain consisted of the fluid domain Ω_f and the solid domain Ω_s with the porous medium domain Ω of small phase dependent permeability $\alpha_e(\phi)$, we can extend the fluid computing region(Ω_f) into the whole computational domain(Ω). In order to transform the original issue to a more analytic problem, we replace the free boundary of the unknown region by a diffuse interface of small thickness $\epsilon > 0$. Thus we can approximate the perimeter by the well-known Ginzburg–Landau energy [44]. Since a multiple of the perimeter functional is the Γ -limit for $\epsilon \rightarrow 0$ of the Ginzburg–Landau energy, we use $F(\phi)/\epsilon^2 + |\nabla \phi|^2/2$ to replace the perimeter functional $\Gamma(\Omega_f)$ in the original optimization problem Eq. (2). Here $F(\phi)$ is denoted as a potential with two global minima and we focus on a double obstacle potential as

$$F(\phi) := \begin{cases} F_0(\phi), & \text{if } 0 \leq \phi \leq 1, \\ +\infty, & \text{otherwise.} \end{cases} \quad \text{where } F_0(\phi) := \phi^2(1-\phi)^2/4. \quad (3)$$

The design variable ϕ is allowed to take values within the range of $[0, 1]$, rather than being restricted to only 0 and 1. Simultaneously, with the introduction of a diffuse interface approximation, we relax the non-permeability condition across the non-fluid region. The adoption of a diffuse interface helps circumvent sharp interface issues, as the latter can impose a substantial computational burden and result in numerical oscillations. Furthermore, we aim to optimize the heat exchanger for thermal fluids based on the TPMS-type channel. In order to force the optimized structure to satisfy the properties of the TPMS, i.e. constant mean curvature, we modify the energy cost functional by introducing the Ginzburg–Landau energy as follows:

$$\mathcal{E}(\phi) = \int_{\Omega} \left(\frac{F(\phi)}{\epsilon^2} + \frac{|\nabla \phi|^2}{2} + \lambda \frac{g(\phi)}{\sqrt{2\epsilon}} \right) d\mathbf{x}. \quad (4)$$

Some notations on the Ginzburg–Landau energy is briefly reviewed here. We introduce ϕ as the phase variable, whose value changes from 0 to 1. Thus we can use $\phi(\mathbf{x})$ to distinguish the interior of the structure as $\{\mathbf{x} : \phi(\mathbf{x}) > 0.5\}$ and the exterior of the structure as $\{\mathbf{x} : \phi(\mathbf{x}) < 0.5\}$. Referring to the established AC-type equation [45] for the mean curvature modification, we begin from $\phi_t = |\nabla \phi|(\kappa(\phi) - \lambda(\phi))$, where $\nabla \phi$ is the norm of the gradient of the ϕ , $\kappa(\mathbf{x}) = \nabla \cdot (\nabla \phi / |\nabla \phi|)$ is the mean curvature at point \mathbf{x} on the surface, and $\lambda(\mathbf{x}) = \int_{\Gamma} \kappa ds / \int_{\Gamma} ds = \int_{\Omega} \kappa \delta(\phi) d\mathbf{x} / \int_{\Omega} \delta(\phi) d\mathbf{x}$ is the average value of the mean curvature over the surface. Here we use the Dirac delta function $\delta(\phi) = |\nabla \phi|$ to avoid the singular solution for the average value of the mean curvature [46]. Our goal is to achieve $\kappa(\phi) = \lambda$ for all points over the surfaces. By the heuristic method in [47], we derive the equilibrium profile $F(\phi) = \phi^2(1-\phi)^2/4 \approx \epsilon^2 |\nabla \phi|^2/2$ based on the variational level-set model. By using this property and the regularized Dirac delta function, we can rewrite κ and λ as follows:

$$\kappa = \nabla \left(\frac{1}{|\nabla \phi|} \right) \cdot \nabla \phi + \frac{\Delta \phi}{|\nabla \phi|} = -\frac{(1-2\phi)}{\sqrt{2\epsilon}} + \frac{\sqrt{2\epsilon} \Delta \phi}{\phi(1-\phi)} = \frac{1}{|\nabla \phi|} \left(-\frac{F'(\phi)}{\epsilon^2} + \Delta \phi \right), \quad (5a)$$

$$\lambda = \frac{\int_{\Omega} \kappa |\nabla \phi| d\mathbf{x}}{\int_{\Omega} |\nabla \phi| d\mathbf{x}} = \frac{\sqrt{2} \int_{\Omega} (-F'(\phi) + \epsilon^2 \Delta \phi) d\mathbf{x}}{\epsilon \int_{\Omega} \phi(1-\phi) d\mathbf{x}} = \frac{-\sqrt{2} \int_{\Omega} F'(\phi) d\mathbf{x}}{\epsilon \int_{\Omega} \phi(1-\phi) d\mathbf{x}}. \quad (5b)$$

Thus the modified Allen–Cahn type equation can be summarized as

$$\phi_t = |\nabla \phi|(\kappa(\phi) - \lambda) = -\frac{F'(\phi)}{\epsilon^2} + \Delta \phi - \lambda \frac{\phi(1-\phi)}{\sqrt{2\epsilon}}, \quad (6)$$

which can be obtained by the variational gradient flow method directly from the energy cost functional Eq. (4) if we chose $g(\phi) = \phi^2/2 - \phi^3/3$. Furthermore, we introduce the following Lagrangian penalty term to force the optimized phase field satisfy $\kappa = \lambda$ without drastic topological changes:

$$\mathcal{L}(\phi) = \int_{\Omega} \frac{\beta}{2} (\psi(\mathbf{x}) - \phi(\mathbf{x}))^2 d\mathbf{x}, \quad (7)$$

where β is a positive Lagrangian multiplier and $\psi(\mathbf{x})$ is the TPMS-based reference structure. We should note that $\psi \in \{0, 1\}$ is not time dependent and given as the combination of various TPMS structures before the calculation. The interior of the channel is set as $\{\mathbf{x} : \psi(\mathbf{x}) = 1\}$ and the exterior of the channel is set as $\{\mathbf{x} : \psi(\mathbf{x}) = 0\}$. Thus the constrained topology optimization problem for the TPMS-based convective heat transfer and composite structure design can be summarized as

$$\begin{aligned} \min_{\Omega} \mathcal{J}_{\text{mod}}(\phi, \mathbf{u}, T) = & \underbrace{\int_{\Omega} \left(\frac{\eta(T)}{2} |\nabla \mathbf{u}|^2 - \mathbf{u} \cdot \mathbf{f} \right) d\mathbf{x}}_{\text{Term A}} + \underbrace{\int_{\Omega} \frac{\alpha_e(\phi)}{2} |\mathbf{u}|^2 d\mathbf{x}}_{\text{Term B}} + \underbrace{\int_{\Omega} \frac{k(T)}{2} |T|^2 d\mathbf{x}}_{\text{Term C}} \\ & + \underbrace{\gamma \int_{\Omega} \left(\frac{F(\phi)}{\epsilon^2} + \frac{|\nabla \phi|^2}{2} + \lambda \frac{g(\phi)}{\sqrt{2\epsilon}} \right) d\mathbf{x}}_{\text{Term D}} + \underbrace{\int_{\Omega} \frac{\beta}{2} (\psi - \phi)^2 d\mathbf{x}}_{\text{Term E}}, \end{aligned} \quad (8)$$

subject to

$$\frac{\partial \phi(\mathbf{x}, t)}{\partial t} = -\gamma \left(\frac{F'(\phi(\mathbf{x}, t))}{\epsilon^2} - \Delta \phi(\mathbf{x}, t) + \lambda \frac{\phi(1-\phi)}{\sqrt{2\epsilon}} \right) + \beta (\psi(\mathbf{x}) - \phi(\mathbf{x}, t)) - \frac{\alpha'_e(\phi)}{2} |\mathbf{u}(\mathbf{x}, t)|^2, \quad (9a)$$

$$\frac{\partial \mathbf{u}(\mathbf{x}, t)}{\partial t} = -\nabla p(\mathbf{x}, t) + \nabla \cdot \left(\eta(T) \nabla \mathbf{u}(\mathbf{x}, t) \right) - \alpha_e(\phi) \mathbf{u}(\mathbf{x}, t) + \mathbf{f}(\mathbf{x}), \quad (9b)$$

$$\nabla \cdot \mathbf{u}(\mathbf{x}, t) = 0, \quad (9c)$$

$$\frac{\partial T(\mathbf{x}, t)}{\partial t} + \mathbf{u}(\mathbf{x}, t) \cdot \nabla T(\mathbf{x}, t) = \nabla \cdot (k(T) \nabla T(\mathbf{x}, t)). \quad (9d)$$

In order to clearly illustration of the energy values in the objective function, we make the explanations on the individual terms as: Term A is the compliance energy for the Stokes flow, where \mathbf{f} is the external force. Term B is the knit energy, which confirm that the velocity is small enough in the porous medium ($\phi = 0$) and satisfies $\lim_{\epsilon \rightarrow 0} \mathbf{u} = \mathbf{0}$. Term C is the thermal energy, where T is the temperature field. Term D is the Ginzburg–Landau energy, which is used to represented the perimeter penalization. Here $\gamma > 0$ is the weighting parameter that determines the significance of the perimeter constraint in the optimization problem. Term E is employed to restrict the volume friction while concurrently mitigating uncertainty in the topological optimization process by taking the reference data ψ . Here β is a positive parameter, which limits the influence of the volume constraint and can be chosen corresponding to the application. Some notations for the proposed model should be remarked: (i) The phase dependent permeability $\alpha_e(\phi) : [0, 1] \rightarrow [0, \tilde{\alpha}_e]$ is surjective, continuous, and decreasing for ϵ , where $(\tilde{\alpha}_e)^{-1} \geq 0$ is the permeability tensor of Darcy's law. Considering the well-posedness of the porous medium model, we should assume $\lim_{\epsilon \rightarrow 0} \tilde{\alpha}_e < \infty$ and $\tilde{\alpha}_e = o(\epsilon^{-\frac{2}{3}})$ [48]. In this paper, we set $\alpha_e(\phi) = \tilde{\alpha}_e(1-\phi)$ for all cases. (ii) In order to consider the influence of temperature gradient on the momentum and heat conduction, we assume that the viscosity and thermal conductivity are both temperature dependent referring to the Sutherland law [49] and can be computed as:

$$\eta(T) = \eta_0 \left(\frac{T}{T_0} \right)^{\frac{3}{2}} \frac{T_0 + 110.4}{T + 110.4}, \quad (10)$$

$$k(T) = \frac{\eta(T)\omega}{(\omega - 1)\Pr}, \quad (11)$$

where η_0 is the dynamic viscosity constant, T_0 is the ambient temperature, ω is the adiabatic index and \Pr is the Prandtl number. The coupled configuration is considered as a 'two-way' profile, which indicates that the kinetic energy and internal energy are interchangeable. (iii) The local optimization problem is transformed into the global optimization problem by taking the Brinkman method with a friction term $\alpha_e(\phi)\mathbf{u}$ in Stokes equation, which indicates that Ω_s and Ω_f are no longer distinguished, we only apply optimization and computation in a porous medium domain Ω . The Brinkman friction term is applied to represent the friction force exerted on a fluid flow when passing through an idealized porous medium [50], which facilitates modeling the topology optimization for the thermal-hydrodynamic problems. (iv) For choosing the values of β and γ , we conduct the following analysis: If β is chosen in the flat region of α_e , it leads to $\alpha_e \approx 0$. Furthermore, by choosing β small enough, the constant porous material can be achieved by setting $\phi = \beta$ and having a very small potential power. Hence, we suggest that $\beta = 1$ is at least suitable for computation. The choice of γ is associate with the formation of the permeability, which has been described in [16]. Therefore, we can set the corresponding weight coefficients based on the material permeability. In this paper, we adopt $\gamma = 0.5$ as a dimensionless parameter for the calculation. Herein, we have described the establishment of the topology optimization governing equations under the thermal conductive and hydrodynamic influence based on the TPMS channels. Compared to alternative frameworks, the proposed method stands out in terms of advantages and innovations, as outlined below: (i) We derive the curvature conservation constraint through the negative gradient variational approach, coupling it with the governing equations for fluid flow and heat transfer. This establishes the

mathematical model for the optimization problem. (ii) We incorporate data from the TPMS structure into the topology optimization problem of thermal fluid flow, ensuring that the optimized pipeline structure satisfies circulation conditions while adhering to fundamental minimal surface morphology. (iii) We establish the corresponding second-order discrete system for both time and space accuracy, which is completely decoupled and linear for computational efficiency. In the subsequent section, we will introduce a theorem on the unconditional stability of energy. This is crucial for scientific computing in hybrid and highly decoupled systems.

Theorem 1. *The solutions to system (Eqs. (9)) satisfy the energy dissipation law, i.e.:*

$$\frac{d\mathcal{J}}{dt} = -(\mathbf{u}_t, \mathbf{u}_t) - k^2(\nabla T, \nabla T) - (\phi_t, \phi_t) \leq 0, \quad (12)$$

where the energy is defined as

$$\begin{aligned} \mathcal{J}(\phi, \mathbf{u}, T) = & \frac{\eta}{2} \|\nabla \mathbf{u}\|^2 - (\mathbf{u}, \mathbf{f}) + \left(\frac{\alpha_\epsilon(\phi)}{2} |\mathbf{u}|^2, \mathbf{1} \right) + \frac{k}{2} \|T\|^2 \\ & + \gamma \left(\frac{F(\phi)}{\epsilon^2} + \frac{|\nabla \phi|^2}{2} + \lambda \frac{g(\phi)}{\sqrt{2\epsilon}}, \mathbf{1} \right) + \frac{\beta}{2} \|\psi - \phi\|^2. \end{aligned} \quad (13)$$

The main conclusion of **Theorem 1** is presented here. The detailed proof processes can be found in [Appendix](#).

Before we delve into the presentation of the solution methodology and proceed with numerical validation, it is essential to provide commentary on the proposed method. Designing internally complicated topological shapes for heat exchange pipelines constitutes a multidisciplinary cross-cutting issue. We incorporate the foundational structural data of TPMS as the reference structure, a concept benefiting from data assimilation methods to restrict excessive topological variations within the pipeline, as discussed in [39]. This approach falls within the domain of shape optimization, aiming to adjust the geometric shape of the structure to meet the connectivity of the flow. Moreover, it is essential to consider the smooth flow of fluid within the pipeline and maximize heat dissipation performance. This necessitates the adjustment of the overall layout of the pipeline structure by redesigning material distribution, and this is precisely where the expertise of topology optimization comes into play [51]. Acknowledging the respective merits of both methodologies, it is imperative to recognize that the methodologies in this paper embody a composite approach, leveraging the dual characteristics inherent in both topology optimization and shape optimization.

3. Discrete system and numerical solutions

In this section, we establish the discrete schemes for solving the composite governing equations and provide the numerical implements for the computation.

3.1. Second order numerical scheme with unconditional stability

Let us first introduce the discrete operators and formulations with the second order central difference method. We illustrate the discrete system by considering the 2D domain $\Omega_p^d = [0, L_x] \times [0, L_y]$, which can be directly conducted to the 3D domain in the same manner. We discretize the computational domain with a uniform mesh grid, whose mesh size is computed as $h = L_x/N_x = L_y/N_y$ with the positive even integers N_x and N_y on the x - and y -directions, respectively. Let us denote i and j as the directional index, thus we can define ϕ_{ij}^n as the approximation to $\phi(x_i, y_j, n\Delta t)$, where $x_i = (i - 0.5)h$, $y_j = (j - 0.5)h$, $\Delta t = T/N$, T is the final time, and N is the total time steps. We denote ∇_d , ∇_d' , and Δ_d as the discrete gradient, divergence, and Laplace operator, respectively. Considering the dissipation of the original energy and avoiding numerical oscillation caused by nonlinearity, we take the Lagrange multiplier method [52] and establish the second-order temporal accurate scheme based on Crank–Nicolson method as follows:

$$\begin{aligned} \frac{\phi^{n+1} - \phi^n}{\Delta t} = & \gamma \Delta_d \phi^{n+\frac{1}{2}} + \beta(\psi - \phi^{n+\frac{1}{2}}) - \frac{\alpha'(\phi^n) + \alpha'(\phi^{n+1})}{4} \frac{|\mathbf{u}^n|^2 + |\mathbf{u}^{n+1}|^2}{2} \\ & - \xi^{n+\frac{1}{2}} \frac{\delta W(\tilde{\phi}^{n+\frac{1}{2}})}{\delta \phi}, \end{aligned} \quad (14a)$$

$$\left(W(\phi^{n+1}) - W(\phi^n), \mathbf{1} \right)_d = \xi^{n+\frac{1}{2}} \left(\frac{\delta W(\tilde{\phi}^{n+\frac{1}{2}})}{\delta \phi}, \phi^{n+1} - \phi^n \right)_d, \quad (14b)$$

$$\frac{\mathbf{u}^{n+1} - \mathbf{u}^n}{\Delta t} + \nabla_d p^{n+\frac{1}{2}} - \nabla_d \cdot \left(\tilde{\eta}^{n+\frac{1}{2}} \nabla_d \mathbf{u}^{n+\frac{1}{2}} \right) + \frac{\alpha(\phi^n) + \alpha(\phi^{n+1})}{2} \mathbf{u}^{n+\frac{1}{2}} = \mathbf{f}, \quad (14c)$$

$$\nabla_d \cdot \mathbf{u}^{n+1} = 0, \quad (14d)$$

$$\frac{T^{n+1} - T^n}{\Delta t} + \mathbf{u}^{n+\frac{1}{2}} \cdot \nabla_d T^{n+\frac{1}{2}} = \nabla_d \cdot \left(\tilde{k}^{n+\frac{1}{2}} \nabla_d T^{n+\frac{1}{2}} \right). \quad (14e)$$

Here we denote $(\tilde{\cdot})^{n+\frac{1}{2}} = 3(\cdot)^n/2 - (\cdot)^{n-1}/2$, $(\cdot)^{n+\frac{1}{2}} = (\cdot)^{n+1}/2 + (\cdot)^n/2$. We have introduced the intermediate variable $W(\phi) = \gamma F(\phi)/\epsilon^2 + \gamma \lambda g(\phi)/(\sqrt{2\epsilon})$ to substitute the nonlinear term. We introduce the time dependent Lagrange multiplier $\xi(t)$ to enforce the dissipation of the original energy. To avoid the nonlinear calculation in Eq. (14a), we use the following formula

$$\frac{\delta W(\tilde{\phi}^{n+\frac{1}{2}})}{\delta \phi} = \gamma \frac{F'(\tilde{\phi}^{n+\frac{1}{2}})}{\epsilon^2} + \gamma \lambda \frac{\tilde{\phi}^{n+\frac{1}{2}}(1 - \tilde{\phi}^{n+\frac{1}{2}})}{\sqrt{2\epsilon}}, \quad (15)$$

with the updated Lagrangian multiplier $\xi^{n+\frac{1}{2}}$ by using Eq. (14b).

Theorem 2. The solutions of the discrete system (Eqs. (14)) satisfies the energy dissipation law, i.e.

$$\mathcal{J}^{n+1} - \mathcal{J}^n = -\frac{1}{\Delta t} \left\| \phi^{n+1} - \phi^n \right\|_d^2 - \frac{1}{\Delta t} \left\| \mathbf{u}^{n+1} - \mathbf{u}^n \right\|_d^2 - \Delta t \left(\tilde{k}^{n+\frac{1}{2}} \right)^2 \left\| \nabla_d T^{n+\frac{1}{2}} \right\|_d^2 \leq 0, \quad (16)$$

where the discrete energy is defined as

$$\begin{aligned} \mathcal{J}_d(\phi^n, \mathbf{u}^n, T^n) &= \tilde{\eta}^{n+\frac{1}{2}} \left\| \nabla_d \mathbf{u}^n \right\|_d^2 / 2 - (\mathbf{u}^n, \mathbf{f})_d + (\alpha_e(\phi^n) |\mathbf{u}^n|^2 / 2, \mathbf{1})_d \\ &\quad + \tilde{k}^{n+\frac{1}{2}} \|T^n\|_d^2 / 2 + \gamma \left(\frac{F(\phi^n)}{\epsilon^2} + \frac{|\nabla_d \phi^n|_d^2}{2} + \lambda \frac{g(\phi^n)}{\sqrt{2\epsilon}}, \mathbf{1} \right)_d + \frac{\beta}{2} \|\psi - \phi^n\|_d^2. \end{aligned} \quad (17)$$

To ensure the fluency of the text, the proof process of **Theorem 2** will be placed in [Appendix](#). Readers can refer to the detailed derivation in [Appendix](#). Several notations should be clarified: (i) The modified discrete equations by the Lagrangian multiplier method is equivalent to the original equation since $d \int_{\Omega} W(\phi) dx / dt = \xi(t) \int_{\Omega} W'(\phi) \phi_t dx$ with $\xi(t) \equiv 1$. (ii) The proposed method can directly prove the original discrete energy dissipation, which avoids the construction of the modified energy like the projection method [53,54] or the auxiliary variable based type method [55,56]. (iii) The Lagrange multiplier $\xi(t)$ is time dependent only, which is mainly used to modify the truncation error caused by the different time steps for the phase variable ϕ^{n+1} and the nonlinear term $W(\tilde{\phi}^{n+\frac{1}{2}})$. (iv) We prove the unconditional energy stability with the time-only discrete schemes, which can be extended to the consistent finite dimensional Galerkin type approximations directly.

3.2. Numerical implements

In order to compute ϕ^{n+1} , \mathbf{u}^{n+1} and T^{n+1} with the given initial ϕ^n , \mathbf{u}^n and T^n , we demonstrate the outline of the main algorithm:

Step 1. Give the reference channel structure ψ and initialize the phase variable ϕ^0 , velocity field \mathbf{u}^0 , the pressure field p^0 , and the temperature field T^0 .

Step 2. Update the temperature dependent viscosity parameter and the thermal conductivity parameter as

$$\tilde{\eta}^{n+\frac{1}{2}} = \eta_0 \left(\frac{\tilde{T}^{n+\frac{1}{2}}}{T_0} \right)^{\frac{3}{2}} \frac{T_0 + 110.4}{\tilde{T}^{n+\frac{1}{2}} + 110.4}, \quad (18)$$

$$\tilde{k}^{n+\frac{1}{2}} = \frac{\tilde{\eta}^{n+\frac{1}{2}} \omega}{(\omega - 1) \text{Pr}}. \quad (19)$$

Step 3. Take the divergence operator in both sides of Eq. (14c) and obtain the Poisson-type equation. We take the Picard iteration method for Eqs. (14a) and (14c) and update the ϕ^{n+1} and \mathbf{u}^{n+1} as follows:

$$\begin{aligned} \frac{\phi^{n+1,m+1} - \phi^n}{\Delta t} &= \frac{\gamma}{2} \Delta_d(\phi^{n+1,m} + \phi^n) + \beta \left(\psi - \frac{\phi^{n+1,m} + \phi^n}{2} \right) \\ &\quad - \frac{\alpha'(\phi^n) + \alpha'(\phi^{n+1})}{4} \frac{|\mathbf{u}^n|^2 + |\mathbf{u}^{n+1,m}|^2}{2} - \xi^{n+\frac{1}{2}} \frac{\delta W(\tilde{\phi}^{n+\frac{1}{2}})}{\delta \phi}, \end{aligned} \quad (20a)$$

$$\Delta_d p^{n+\frac{1}{2}} = \nabla_d \cdot \mathbf{f} - \frac{1}{4} \nabla_d \left(\alpha(\phi^n) + \alpha(\phi^{n+1,m+1}) \right) \cdot (\mathbf{u}^{n+1,m} + \mathbf{u}^n), \quad (20b)$$

$$\begin{aligned} \frac{\mathbf{u}^{n+1,m+1} - \mathbf{u}^n}{\Delta t} &= -\nabla_d p^{n+\frac{1}{2}} + \frac{1}{2} \nabla_d \cdot \left(\tilde{\eta}^{n+\frac{1}{2}} \nabla_d (\mathbf{u}^{n+1,m} + \mathbf{u}^n) \right) \\ &\quad - \frac{1}{4} (\alpha(\phi^n) + \alpha(\phi^{n+1,m+1})) (\mathbf{u}^{n+1,m} + \mathbf{u}^n) + \mathbf{f}. \end{aligned} \quad (20c)$$

where m is the index of Picard iteration. The initial conditions are chosen as $\phi^{n+1,0} = 2\phi^n - \phi^{n-1}$, $\mathbf{u}^{n+1,0} = 2\mathbf{u}^n - \mathbf{u}^{n-1}$. The computation is performed until the error is smaller than a given tolerance as

$$\left\| \phi^{n+1,m+1} - \phi^{n+1,m} \right\|_d^2 + \left\| \mathbf{u}^{n+1,m+1} - \mathbf{u}^{n+1,m} \right\|_d^2 < tol. \quad (21)$$

Then, we will set $\phi^{n+1} = \phi^{n+1,m+1}$ and $\mathbf{u}^{n+1} = \mathbf{u}^{n+1,m+1}$.

Step 4. Update the Lagrangian multiplier $\xi^{n+\frac{1}{2}}$ by solving Eq. (22):

$$\left(W(\phi^{n+1}) - W(\phi^n), \mathbf{1} \right)_d = \xi^{n+\frac{1}{2}} \left(\frac{\delta W(\tilde{\phi}^{n+\frac{1}{2}})}{\delta \phi}, \phi^{n+1} - \phi^n \right)_d. \quad (22)$$

Step 5. Update the temperature field with Eq. (14e) as:

$$\frac{T^{n+1,q+1} - T^n}{\Delta t} = \frac{1}{2} \nabla_d \cdot \left(\tilde{k}^{n+\frac{1}{2}} \nabla_d (T^{n+1,q+1} + T^n) \right) - \frac{1}{4} (\mathbf{u}^{n+1} + \mathbf{u}^n) \cdot \nabla_d (T^{n+1,q} + T^n), \quad (23)$$

where q is the index of the Picard iteration and the computation is applied until the error satisfies $\|T^{n+1,q+1} - T^{n+1,q}\|_d \leq tol$ with the initial condition $T^{n+1,0} = 2T^n - T^{n-1}$. Thus we set $T^{n+1} = T^{n+1,q+1}$.

Some notations should be summarized as follows: (i) Due to the highly coupled property, the Picard iterations are essential to linearize the governing equations. The residual error converges quickly to a tolerance $tol = 1e - 6$ in 3-5 iterations for every Picard iteration. (ii) The central difference scheme is used for the second-order spatial discretization. We perform a nonlinear full approximation storage multigrid method at the implicit time step for solving the Poisson-type pressure Eq. (20b). The computational complexity is only $O(N_h)$, where N_h is the size of mesh grid. (iii) The existence of the unique solutions to the governing equations can be guaranteed since Eqs. (20a), (20b), (20c), and (23) is a linear system of $\phi^{n+1,m+1}$, $\mathbf{u}^{n+1,m+1}$, $p^{n+\frac{1}{2}}$, and $T^{n+1,m+1}$, respectively. The computational cost of the proposed algorithm is equivalent to that with explicit algorithm. (iv) The complexity of the Eq. (22) depends on $W(\phi)$, which is a forth-order algebraic equation for $\xi^{n+\frac{1}{2}}$ and has various solutions. Since we want to find the solutions approximates to $\xi^{n+\frac{1}{2}} = 1$, it can quickly convergence by using $\xi^0 = 1$ with the Newton iteration.

4. Numerical tests and discussions

In this section, we present various numerical tests from both qualitative and quantitative perspectives to demonstrate the robustness of the proposed method. Unless otherwise specified, we choose the computational domain as $\Omega^d = [0, 10] \times [0, 20]$ with a 256×512 mesh grid in two dimensional space and $\Omega^d = [0, 10] \times [0, 10] \times [0, 20]$ with a $128 \times 128 \times 256$ mesh grid in three dimensional space. We choose the following parameters for the numerical simulations: $\gamma = 0.5$, $\beta = 1$, $\alpha_e = 10$, $\epsilon = 4h/(4\sqrt{2}\text{atanh}(0.9))$, $\eta_0 = 1.85e - 5$, $T_0 = 25$, $\omega = 1.4$, $Pr = 0.72$, $\Delta t = 0.1h$. We perform the Neumann boundary conditions perpendicular to the direction of flow for the phase-field ϕ , the velocity field \mathbf{u} , the pressure field p , and the temperature field T . For the inlets and outlets of the optimized channels, we apply the Dirichlet boundary conditions.

4.1. Two dimensional tests under various TPMS-based structures

We demonstrate various two dimensional tests under different TPMS-based scenarios. We first consider the aimed channel is composed by the Primitive-type structures with gradient porosity. We assume that the inlet is at the top and the outlet is at the bottom of the channel. The initial conditions are chosen as

$$\phi(x, y, 0) = \text{rand}(x, y), \quad T(x, y, 0) = 10\psi(x, y), \quad \mathbf{u}(x, y, 0) = (0, -10\psi(x, y)). \quad (24)$$

Based on the random initial conditions, we plot the evolution and results during the optimized process as shown in Fig. 2. The CPU time utilized in this test is 7.38 s. As can be seen from the reference structure in Fig. 2, the solid–fluid interface of the new structure obtained by directly merging two Primitive-structures with different porosity is rough with sharp corners. The evolution part demonstrate the shape optimization process, which can indicate that the proposed method works well for smoothing the channel shape and forcing the surface curvature to be constant. Then the temperature field and the velocity field have been demonstrated in Fig. 2. It is obvious that the heat flux conducts over the channel interface in the direction of the temperature gradient. From the plotted velocity field, we can see that the velocity norm is high at narrow region compared with that at wide region, which corresponds to the Bernoulli's principle [57]. Then we consider the shape topology optimization based on the combination of Primitive and Gyroid structures. As depicted in Fig. 3, we combine Primitive-type and Gyroid-type structures to design an adapted channel, with a CPU time of 6.29 s. Due to the structural differences between the Primitive unit cell and the Gyroid unit cell, the channel of the composite structure is disconnected and the sharp corners are inevitable, which can be seen from the reference structure in Fig. 3. Due to the effect of the stokes equation, the friction caused by fluid flow and the seepage effect blunt the sharp corners and smooth the fluid domain in the channel. The temperature result indicates the transfer of heat flux from the fluid domain to the solid domain. Comparing to the temperature results in Fig. 2, we can see that the average temperature in the P-G composite channel is lower than that in the P-P composite channel. To facilitate a clearer comparison between these two outcomes, it is essential to highlight the ratio of physical properties between P-P and P-G composite channels: the inlet area ratio is 0.8 : 1, the outlet area ratio is 1.2 : 1, the fluid volume ratio is 1.17 : 1, and the area ratio of the fluid–solid interface is 0.85 : 1, respectively. Therefore, two reasons can be summarized here: (i) The composite channel in Fig. 3 is more complex than that in Fig. 2 and has a larger area of the fluid–solid interface. (ii) Eddies have appeared as the fluid moves through the channel, decreasing the value of the flow velocity and facilitating heat transfer. The subsequent numerical experiments will verify these two reasons through quantitative comparison. Furthermore, we investigate the channel shape topology optimization with two cell size Primitive-type structures as shown in Fig. 4. The computational domain is chosen as $\Omega = [0, 10] \times [0, 15]$ with a 256×384 mesh grid. In contrast to Fig. 2, where the cell size is uniform, the composite structure in this case features a bottom part with cell sizes half that of the top part. This configuration compels the fluid to split into two branches through the interface. The CPU time utilized in this test is 10.84 s. The fluid flow past a circular cylinder splits into two parts since the channel below provides two outlets for the flow rather than the well-known Kármán vortex caused by the vortex shedding [58]. The evolution results demonstrate that the disconnected interface has been dredged under the influence mean curvature effect. In addition, the area of the fluid–solid interface increases compared to the composite structure composed by uniform Primitive structures in Fig. 2, which facilitates heat loss in the fluid domain. According to these two-dimensional results, it is obvious that the proposed method can indeed optimize the shape of the flow channel according to the referred TPMS structures and increase the heat loss.

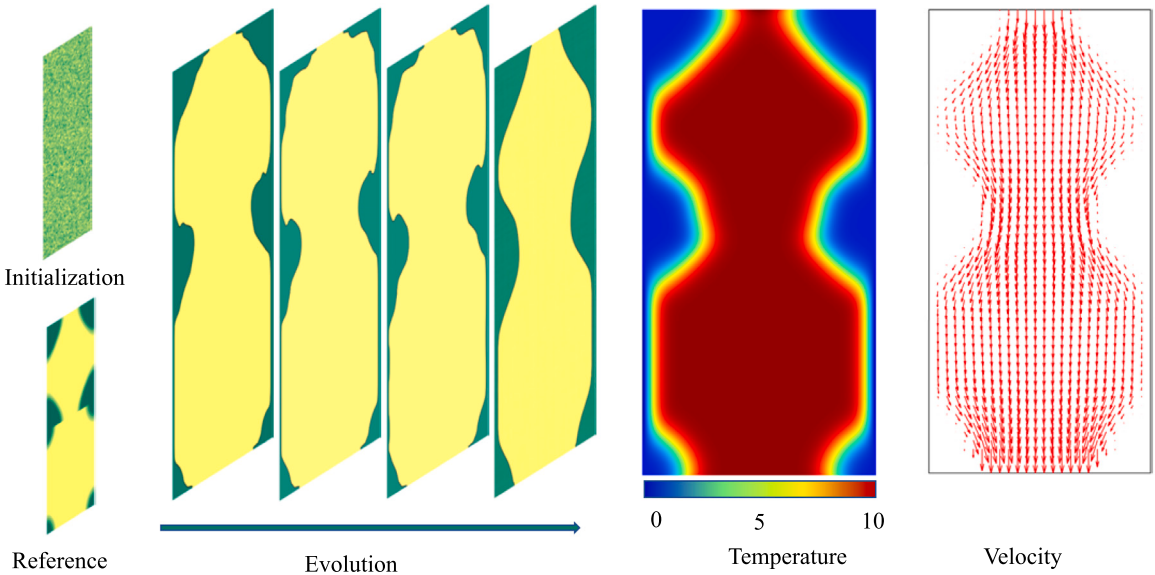


Fig. 2. Schematic illustration of Primitive-based topology optimization with gradient porosity. From left to right, the results are the initialization, reference structure, time evolution of shape optimization, the temperature field, and the velocity field distribution, respectively.

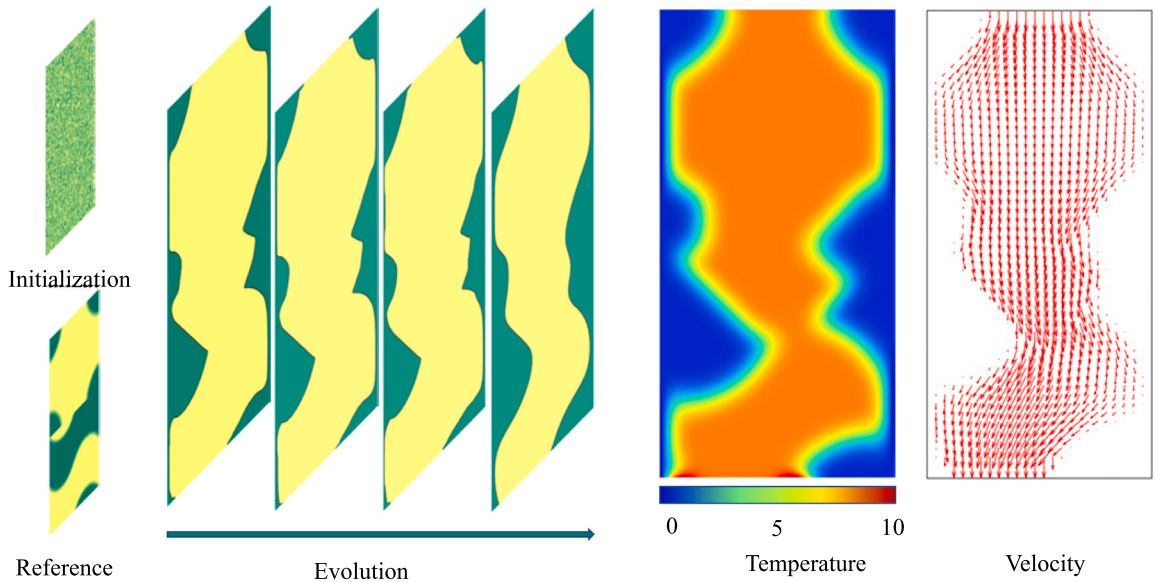


Fig. 3. Schematic illustration of Primitive-Gyroid-based topology optimization. From left to right, the results are the initialization, reference structure, time evolution of shape optimization, the temperature field, and the velocity field distribution, respectively.

4.2. Energy dissipation and stability test

In this subsection, we perform the numerical tests for investigating the unconditional energy dissipation and stability with the above TPMS-based structures. To demonstrate the energy dissipation, we compute the time evolution of the normalized discrete energy $\mathcal{J}_d(\phi^n, \mathbf{u}^n, T^n)/\mathcal{J}_d(\phi^0, \mathbf{u}^0, T^0)$. The chosen computational domain, initial conditions and parameters settings are the same in Section 4.1. As can be seen from Fig. 5(a), the plotted discrete energy curves of the above three cases are indeed non-increasing, which corresponds to the proved Theorem 2. Since the proposed model is composed of the strong nonlinear term and highly coupled term, the numerical solutions is limited by severe temporal restrictions for energy stability. We investigate the energy stability with $\Delta t = 10, 1, 0.1$, and 0.01 under the different TPMS types framework to demonstrate the stability of the proposed numerical scheme. As can be seen from Fig. 5(b), the four energy curves decay unconditionally with respect to time. It is obvious that no blow-up of the numerical solutions occur with the large time step, which suggests that our algorithm is not limited by the temporal step size.

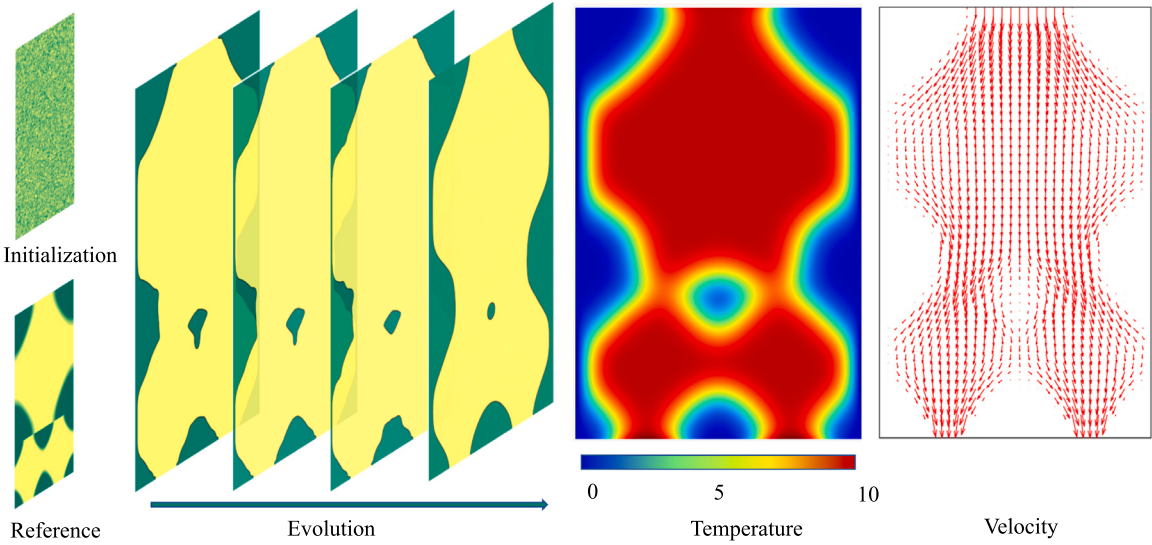


Fig. 4. Schematic illustration of TPMS-based topology optimization with different scale structures. From left to right, the results are the initialization, reference structure, time evolution of shape optimization, the temperature field, and the velocity field distribution, respectively.

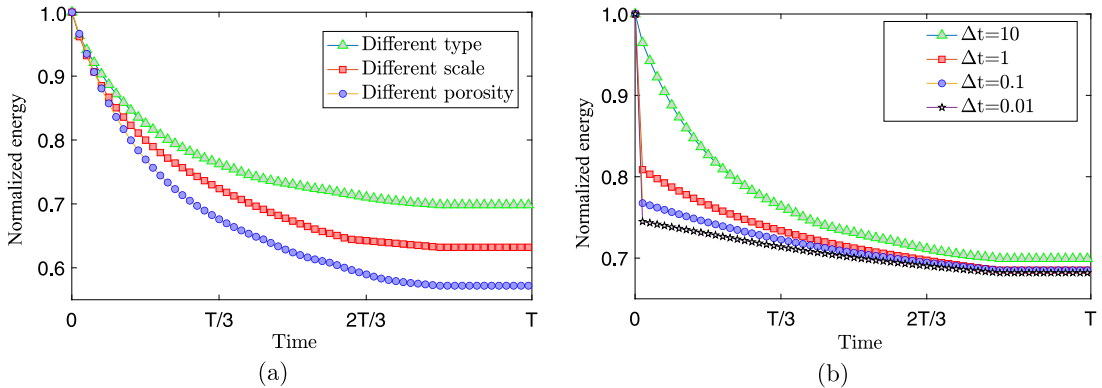


Fig. 5. (a) Temporal evolution of the non-increasing discrete energy based on the TPMS composite structures with different type, different scale, and different porosity. (b) Temporal evolution of the discrete energy under the different TPMS types framework with four time step sizes of $\Delta t = 10, 1, 0.1$, and 0.01 , respectively. Note that the total energy has been normalized by the initial energy.

Comparing the results obtained by using $\Delta t = 10$, we can obviously see that using the small time step can obtain more accurate results since less truncation error of the numerical solutions has been involved. Furthermore, it is obvious that the results with $\Delta t = 0.1$ are in good agreement with the results with $\Delta t = 0.01$. In order to obtain more accurate results with less computational cost, we recommend using $\Delta t = 0.1$ for the numerical scheme.

4.3. Convergence test

In this section, the second order temporal and spacial accuracy of the proposed numerical system have been investigated. The chosen computational domain, initial conditions and parameters settings are the same with Fig. 2 in Section 4.1. Since the absence of the closed-form solution, we use the Euler method to investigate the Cauchy error of our proposed method. First we denote the following reference solution ϕ_{ref} , u_{ref} , v_{ref} , and T_{ref} by using the fine time step or the fine grid size. As shown in Table 1, we use the decreasing temporal steps as $\Delta t = 1e-2$, $5e-3$, and $2.5e-3$ with the fine grid size $h = 10/512$, respectively. The reference solutions are obtained by using $\Delta t = 1e-4$. Thus the numerical errors for phase field variable ϕ are defined as $e_{\phi,\Delta t} := \phi_{\Delta t} - \phi_{\text{ref}}$ and the convergence rate can be defined as $\log_2 \left(\|e_{\phi,\Delta t}\|_2 / \|e_{\phi,\Delta t/2}\|_2 \right)$. The other numerical error and convergence rate for u , v , and T are defined in the same manner. The results presented in Table 1 demonstrate that the temporal accuracy of the proposed method is indeed second-order, which has a good agreement with Eqs. (14). In order to investigate the spatial accuracy of the proposed method, we fix the temporal step size as $\Delta t = 1e-4$ and choose the decreasing grid size as $h = 10/64$, $h = 10/128$, and $h = 10/256$, respectively. The reference solution are obtained by using $h = 10/512$. The spatial error for the phase field variable is defined as

Table 1

Errors and convergence rates with different time steps for velocity field u and v , phase field ϕ and temperature field T .

Δt	Error				Order			
	u	v	ϕ	T	u	v	ϕ	T
1e - 2	8.616e - 02	7.521e - 03	6.316e - 03	9.612e - 03	—	—	—	—
5e - 3	1.841e - 02	1.958e - 03	1.480e - 03	2.499e - 03	2.23	1.94	2.09	1.94
2.5e - 3	4.317e - 03	4.669e - 04	3.556e - 04	5.983e - 04	2.09	2.07	2.06	2.06

Table 2

Errors and convergence rates with different space steps for velocity field u and v , phase field ϕ and temperature field T .

N	Error				Order			
	u	v	ϕ	T	u	v	ϕ	T
64	6.511e - 03	4.816e - 03	7.319e - 04	3.284e - 03	—	—	—	—
128	1.570e - 03	1.102e - 03	1.745e - 04	8.506e - 04	2.05	2.13	2.07	1.95
256	3.943e - 04	2.614e - 04	4.456e - 05	2.053e - 04	1.99	2.08	1.97	2.05

$e_{\phi,h} := \phi_h - \phi_{\text{ref}}$ and the convergence rate is defined as $\log_2 \left(\|e_{\phi,h}\|_2 / \|e_{\phi,h/2}\|_2 \right)$. The other spatial error and convergence rate for other variable are defined in the same manner. The calculated numerical spatial error and convergence rate are presented in [Table 2](#). It is obvious that our method is indeed second order accurate in space.

4.4. Three dimensional optimized channel design with different type TPMS-based structures

In this subsection, we apply the channel optimization with two type TPMS structures to investigate the universality and robustness of the proposed method in three dimensional space. When employing diverse microscopic unit cells, a challenge arises where adjacent volume elements generally exhibit either partial or complete non-matching characteristics, resulting in design failures and unviable manufacturing. These challenges necessitate effective mitigation strategies, systematically explored in recent scholarly works. We contemplate two contiguous cubic volumes and periodic TPMSs sharing a common edge. The objective is to formulate a design methodology for seamlessly integrating P structures and G structures in a continuous and smooth manner. Owing to their advantages of good compactness and stress dispersion, these two structures have found extensive applications in areas such as skeletal repair [59], biomimicry [60], and lightweighting of architectural structures [61] when combined through assembly. Furthermore, the distinctive differences in contact surfaces between these two structures prominently showcase that our algorithm is not constrained by the types of TPMS structures. The initial conditions are chosen as

$$\phi(x, y, z, 0) = \text{rand}(x, y, z), \quad T(x, y, z, 0) = 10\psi(x, y, z), \quad \mathbf{u}(x, y, z, 0) = (0, 0, -10\psi(x, y, z)). \quad (25)$$

The reference structure has been shown as the first subplot in [Fig. 6](#). Let us assume that the fluid with heat enters from the top of the P structures and exits from the bottom of the G structure. By applying our method, the optimized structure can be obtained as shown in the second row of [Fig. 6](#). In order to demonstrate the details inside the composite structure, we select five representative slices along the x -direction to display, the numbers of the chosen slices are 1, 25, 50, 75, and 100, respectively. In this test, the total CPU time utilized amounted to 34.27 s. We plot the 0.5 contour level of the results obtained by our method with red solid lines and obtained by the original structure with blue dashed lines. As can be seen from the comparison results of shape slices in [Fig. 6](#), the contrast changes inside the composite structures demonstrate that our method can indeed effectively improve the internal connectivity. In addition to considering the connectivity of physical shapes, our method also smooths the fluid channel interface under the influence of stokes equations, where no sharp corners and rough surfaces have been hold. In order to demonstrate the velocity field in the composite structure, we plot the velocity streamline in [Fig. 6](#). The numerical representation of streamlines delineates the flux within fluid dynamics, while the chromatic characteristics of the streamlines articulate the thermal values. Warmer coloration aligns with augmented numerical magnitudes, whereas cooler hues align with diminished numerical magnitudes. It is obvious that the fluid directly passes through the Primitive structure from the inlet. However, the vortex has been formed in the Gyroid structure, which slows the fluid flow and facilitates the diffusion of the heat flux. In order to clearly show the velocity field in the whole space, we plot the velocity field on 1, 25, 50, 75, and 100 slices, respectively. The colormap corresponds to the value of the norm of the velocity and the arrow represents the direction of the flow field. As can be seen from the results, we can summarize the following conclusion: (i) The flow velocity at the outlets decrease significantly compared to the flow velocity at the inlets, since the fluid vortex and collision have appeared in the G structure. (ii) The channels designed by our proposed method are indeed connected, in other words, the conservation of fluid flux can be guaranteed. (iii) The proposed method is universal and not limited by the types of the TPMS structures. (iv) The proposed algorithm is based on stokes equation, which can design the optimal channel shape suitable for fluid flow.

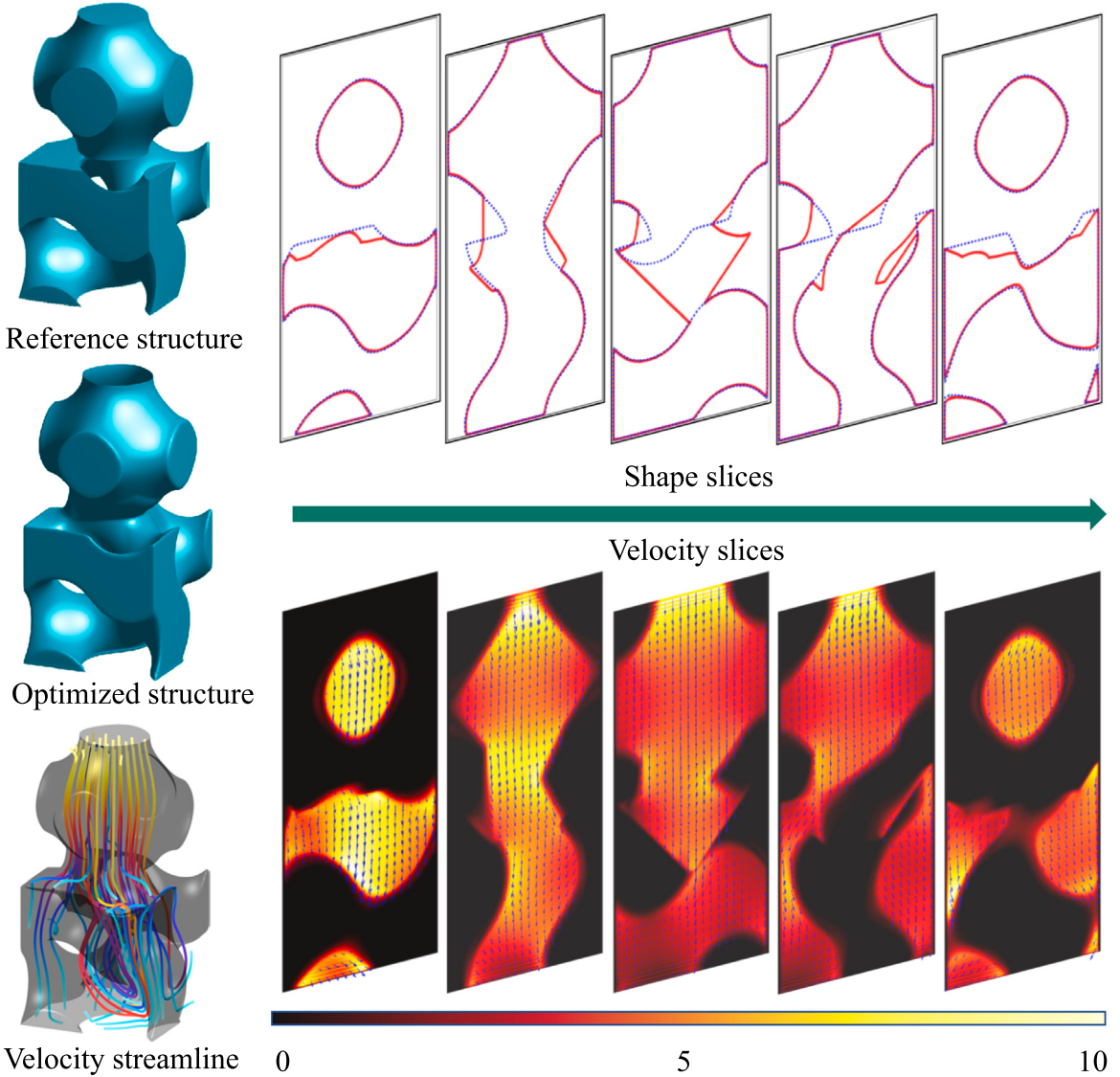


Fig. 6. Three dimensional channel optimization with Primitive and Gyroid structures. The left column shows the reference structure, the optimized structure, and the velocity streamline in the optimized channel. The quantity of streamlines serves as an indicator of fluid flow flux, and the color of the streamlines denotes the temperature values. Warmer hues correspond to elevated numerical values, whereas cooler hues indicate lower numerical values. The right column shows the shape slices and the velocity slices. The red solid lines are the 0.5 contour level of the optimized structures by our method and the blue dashed lines are the 0.5 contour level of the original structure. The colormap corresponds to the value of velocity, and the arrow represents the direction of the flow field.

4.5. The qualitative comparison between the original and the optimized TPMS-based channels

Regular heat exchangers composed of unite TPMS structures have good heat transfer performance, which has been investigated in various state-of-the-art works [62,63]. However, direct combination with TPMS structures limits the heat transfer and flow performance of the channel. In this subsection, we apply the qualitative comparison to investigate the difference between the original structure and the optimized structure with the TPMS structures of the same type and size. In order to demonstrate the fluid flow inside the two channels, we consider the computational domain as $\Omega = [0, 40] \times [0, 10] \times [0, 10]$ with a $512 \times 128 \times 128$ mesh grid and plot the velocity streamlines. The initial conditions are chosen as

$$\phi(x, y, z, 0) = \text{rand}(x, y, z), \quad T(x, y, z, 0) = 10\psi(x, y, z), \quad \mathbf{u}(x, y, z, 0) = (10\psi(x, y, z), 0, 0). \quad (26)$$

We assume the channel structure is arranged at the domain $\Omega_c = [10, 30] \times [0, 10] \times [0, 10]$ with a $256 \times 128 \times 128$ mesh grid and two combined Gyroid structures as the reference structure, which is shown in the cyan structure of Fig. 7(a). We should emphasize that the quantity of streamlines serves as an indicator of fluid flow flux, and the color of the streamlines signifies the temperature values.

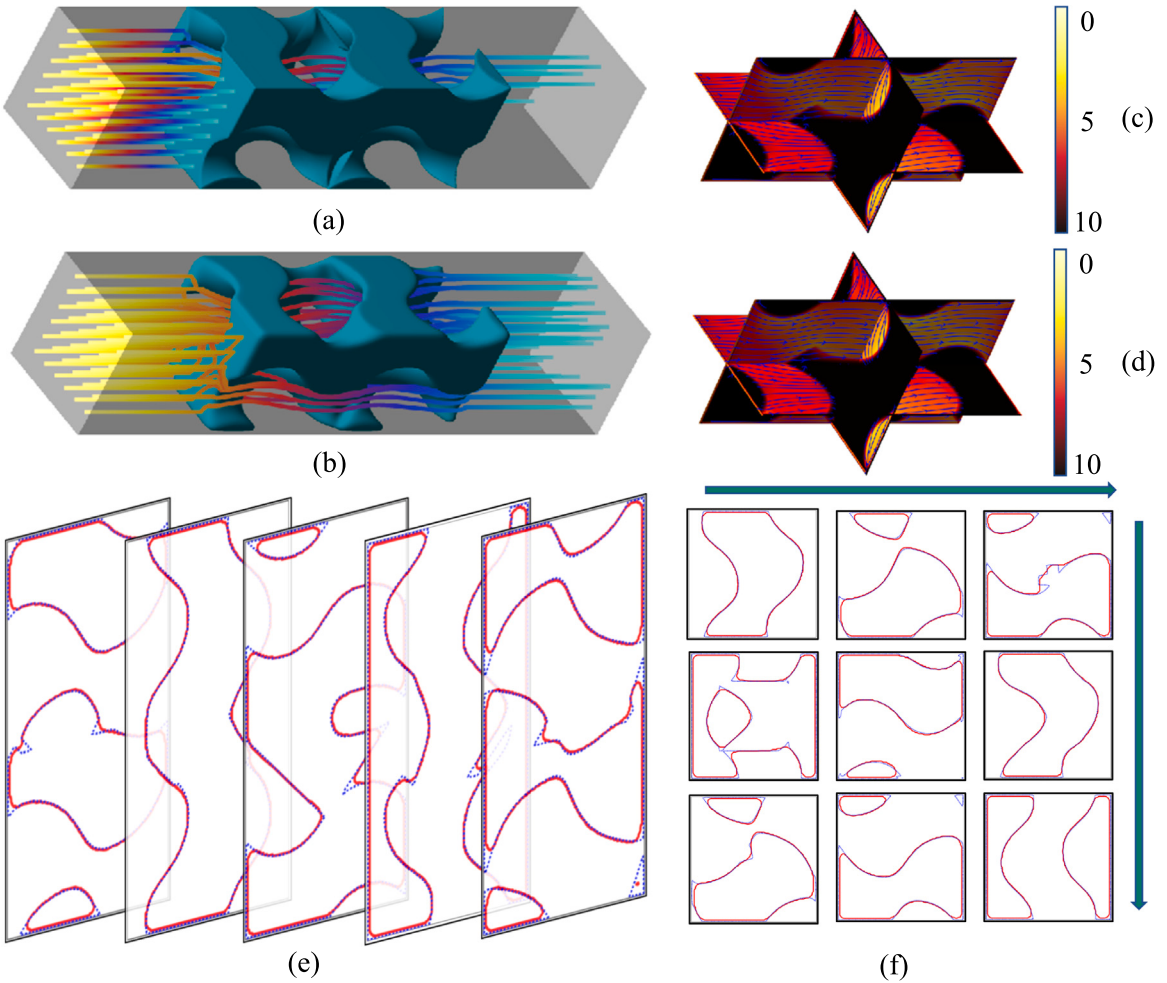


Fig. 7. Comparison results of the channel composed of two Gyroid structures . (a) The original Gyroid-based channel with the velocity streamline. (b) The optimized Gyroid-based channel with the velocity streamline. The quantity of streamlines indicates the fluid flow flux, and the color of the streamlines signifies the temperature value. Warmer colors correspond to higher numerical values, while cooler colors indicate lower numerical values. (c) The contour plot of the velocity field coupled with the stream slice of (a). (d) The contour plot of the velocity field coupled with the stream slice of (b). (e) The 0.5–level contour line of different indicated slices on the x -direction. (f) The 0.5–level contour line of different indicated slices on the z -direction. The red solid lines are the 0.5 contour level of the optimized structures by our method and the blue dashed lines are the 0.5 contour level of the original structure.

Warmer hues correspond to elevated numerical values, whereas cooler hues denote lower numerical values. We obtain the optimized structures by the proposed method as shown in the cyan structure of Fig. 7(b) after the CPU time of 34.27 s. The initial conditions, the parameters settings, and the boundary conditions are chosen the same for the two cases. As can be seen from the comparison results, it is obvious that the optimized channel has the characteristics of increasing fluid flux and smooth surface without sharp corners. In other words, increasing fluid flux means less pressure on the wall of the optimized channel with the same velocity from the inlets. The smooth surfaces make our channels are less prone to wear and tear with the fluid flow in the real word physical context. The contour plot of the velocity field coupled with the stream slice of the original structure and the optimized structure have been shown in Fig. 7(c) and (d), respectively. The colormap corresponds to the value of velocity, and the arrow represents the direction of the flow field. In order to compare the channel shape of the two structures, we select the 0.5–level contour line of the indicated slices 1, 25, 50, 75, and 100 on the x -direction, respectively. Furthermore, we demonstrate the 0.5–level contour line of the indicated slices 1, 25, 50, 75, 100, 125, 150, 175, and 200 on the z -direction, respectively. The red solid lines represent that the results are from the optimized structure and the blue dashed lines represent that the results are from the original structure. The comparison results indicate that our method indeed eliminates the sharp corners and smoothing the channel surface without changing the basic structure shape. In addition, we compare the results using the I-WP structure, as shown in Fig. 8, which incurs a CPU time of 36.18 s. Comparing to the results in Fig. 7, we find that the fluid flux drop by taking the I-WP channel is less than that by taking the Gyroid channel. This is because there are no sharp corners in the original I-WP channel as shown in Fig. 8(e) and (f), our algorithm does not apply large-scale adjustment to obtain the optimized channel. Thus it is obvious that our method works well for the adaptive optimization of the fluid channel while considering the specific situations.

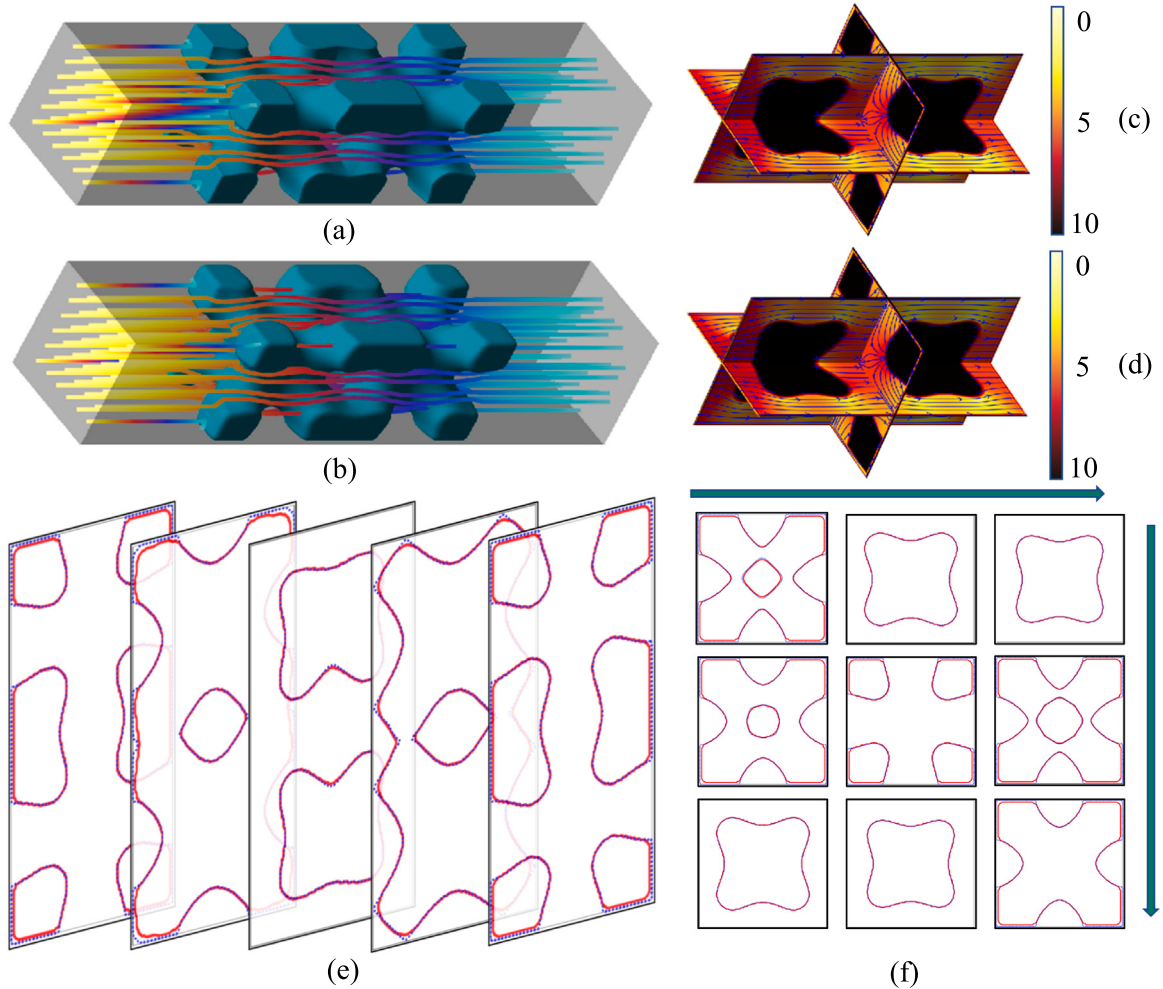


Fig. 8. Comparison results of the channel composed of two I-WP structures . (a) The original I-WP-based channel with the velocity streamline. (b) The optimized I-WP-based channel with the velocity streamline. The number of the streamline indicates the flux of fluids flow and the color of the streamlines signify the temperature value. The warmer colors correspond to higher numerical values, while cooler colors indicate lower numerical values. (c) The contour plot of the velocity field coupled with the stream slice of (a). (d) The contour plot of the velocity field coupled with the stream slice of (b). (e) The 0.5-level contour line of different indicated slices on the x -direction. (f) The 0.5-level contour line of different indicated slices on the z -direction. The red solid lines are the 0.5 contour level of the optimized structures by our method and the blue dashed lines are the 0.5 contour level of the original structure.

4.6. The quantitative comparison between the original and the optimized TPMS-based channels

In this subsection, we performed the quantitative comparison by considering the indicated physical index, such as the specific pressure drop, heat transfer coefficient, and the surface area between fluid domain and solid domain, with different TPMS-based channels. We first take the following definitions. Let us define the volume share as $R = V_f/V_\Omega$, where $V_f = \sum_i^{N_x} \sum_j^{N_y} \phi_{i,j}$ is the volume of the fluid domain and V_Ω is the volume of the whole computational domain. Let us define the pressure drop as $\Delta p = \bar{p}_{out} - \bar{p}_{in}$, where $\bar{p}_{out} = \sum_i^{N_x} \sum_j^{N_y} p_{i,j}^{out}/N_x N_y$ is the average pressure at the outlet and $\bar{p}_{in} = \sum_i^{N_x} \sum_j^{N_y} p_{i,j}^{in}/N_x N_y$ is the average pressure at the inlet. Let us define the heat transfer coefficient as $h_c = q/(T_s - T_f)$, where q is the heat flux and has been chosen as a constant here, $T_s = \sum_i^{N_x} \sum_j^{N_y} T_{i,j}(1 - \phi_{i,j}) / (\sum_i^{N_x} \sum_j^{N_y} (1 - \phi_{i,j}))$ is the average temperature of the solid domain and $T_f = \sum_i^{N_x} \sum_j^{N_y} T_{i,j}\phi_{i,j} / (\sum_i^{N_x} \sum_j^{N_y} \phi_{i,j})$ is the average temperature of the fluid domain. It should be noted that these physical indexes are all dimensionless. The computational domain, parameters settings, and the initial conditions are chosen the same as those in Section 4.4. The fluid channel in the computational domain are composed of two TPMS structures by adding up along the z -direction. The initial velocity and the physical parameters are chosen the same for all cases. As can be seen from the relationship between specific pressure drop and volume share shown in Fig. 9, the pressure drop Δp decreases as the volume share R increase, since the higher value of R indicates a greater hydraulic diameter and a smaller specific surface area. Furthermore, due to the mass flux conservation of the continuity equation, the greater flow velocity will be obtained with smaller R . Due to the double aspects influence of more distinct surface and larger velocity, the fluid acceleration has been aggravated with intensive fluid mixing [62].

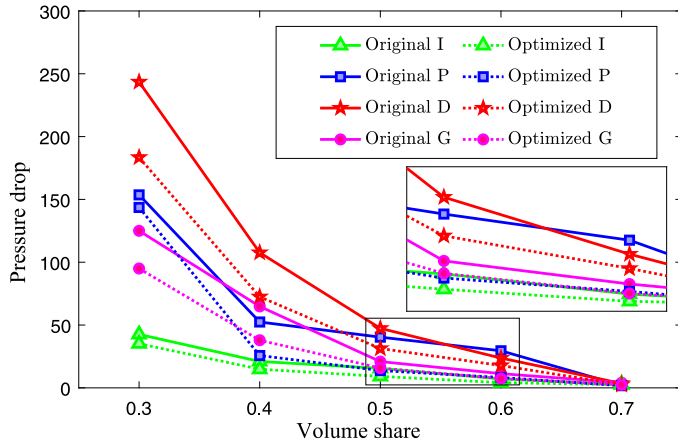


Fig. 9. Comparison results of relationship between specific pressure drop and volume share with different type channels. The solid lines show the results with the original TPMS-based structures. The dashed lines show the results with the optimized TPMS-based structures. The red solid lines are the 0.5 contour level of the optimized structures by our method and the blue dashed lines are the 0.5 contour level of the original structure.

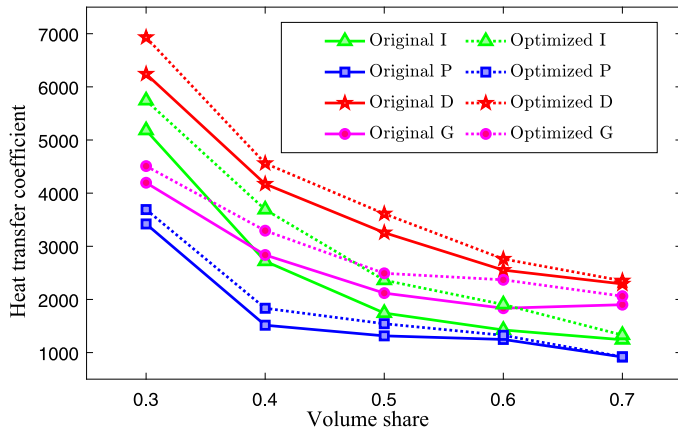


Fig. 10. Comparison results of relationship between heat transfer coefficient and volume share with different type channels. The solid lines show the results with the original TPMS-based structures. The dashed lines show the results with the optimized TPMS-based structures.

Table 3

The comparison results of the surface area on the composite structure composed by different types TPMS structures. The dimensionless size of the composite structure is $100 \times 100 \times 200$.

$\times 10^4$	$P - P$	$G - G$	$D - D$	$I - I$	$P - G$	$G - D$	$G - I$	$P - D$	$P - I$	$D - I$
Original	8.986	9.561	11.148	10.026	9.274	10.355	9.794	10.067	9.506	10.587
Optimized	9.367	10.801	11.772	10.376	10.148	11.938	11.409	11.343	10.582	11.745

Thus the heat transfer coefficient decrease with the increase of R , which has been shown in Fig. 10. As can be seen from Fig. 9, the pressure drop is greatly affected by the channel types when $R \leq 0.4$ and the difference between pressure drops among four type TPMS channels is noticeable. The specific pressure drop of Diamond channel is the largest and the I-WP channel has the smallest value. However, when $R \geq 0.5$, the influence of R on the pressure drop becomes weaker, which even can be ignored when $R = 0.7$. It should be noted that the optimized channel has the lower pressure drop than the original channel for the specific TPMS structure, which indicates that our method can increase connectivity inside the channels. Considering the convective heat transfer, the Diamond channel has the best performance while the Primitive channel has the worst performance due to the differences in topologies. When $R \leq 0.4$, the I-WP channel has the better convective heat transfer than the Gyroid channel while when $R \geq 0.5$, it is the opposite. However, comparing with the specific original channel, the thermal conductivity of the corresponding optimized channel has been improved. Furthermore, we have calculated the surface area on the composite structure composed of TPMS structures with different types. The comparison results have been shown in Table 3. The dimensionless size of the composite structure is $100 \times 100 \times 200$ and the surface area has been computed by the size of the composite structure. As can be seen from the results, the area of the fluid-solid interface can be increased, which is significant for improving the convective heat transfer.

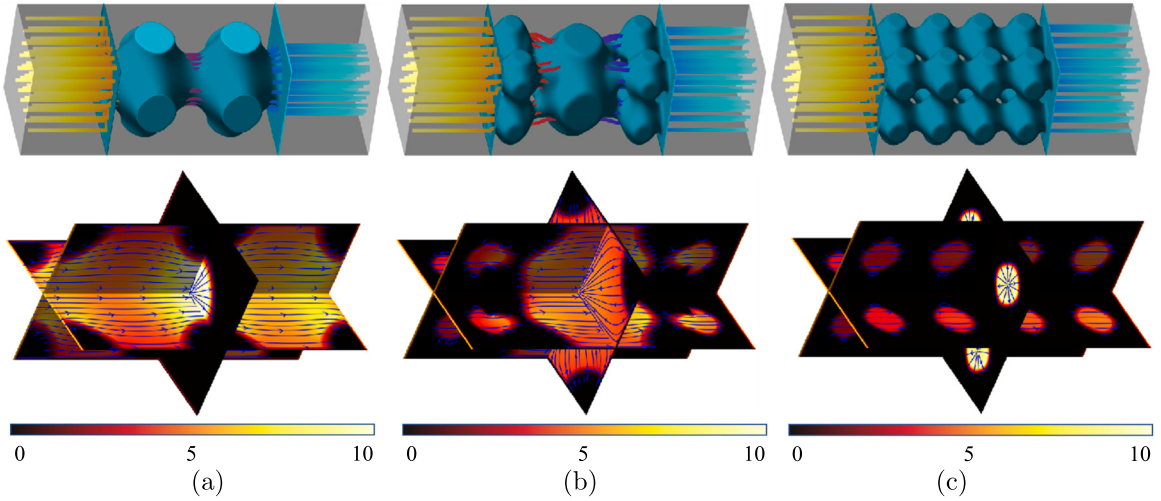


Fig. 11. Comparison results of the channel composed of different scale Primitive structures. The top row shows the velocity streamline. The bottom row shows the contour plot of the velocity field coupled with the stream slice. (a) The uniform big Primitive-based channel. The number of the streamline indicates the flux of fluids flow and the color of the streamlines signify the temperature value. The warmer colors correspond to higher numerical values, while cooler colors indicate lower numerical values. (b) The optimized Primitive-based channel. (c) The uniform small Primitive-based channel.

4.7. The comparison test between the composite structures composed of unit Primitive-based structures with different cell sizes

In this subsection, we are going to conduct a novel type of channel shape with the Primitive structure. As analyzed in the quantitative comparison test, the thermal conduction of Primitive structure is not good, since the internal structure of Primitive channel is simple and there is no fluid–solid cross domain. Furthermore, as can be seen from Table 3, the $P - P$ type composite channel has the smallest surface area, which is not conducive to heat transfer from the fluid domain to the solid domain. Thus we aim to conduct a novel type of channel shape with the Primitive structure by changing the size of the Primitive structure to improve the thermal conductivity of the channel. The computational domain, physical parameters, and the initial conditions are chosen the same as those in Section 4.5. As can be seen from Fig. 11(a) and (c), we demonstrate the uniform big Primitive based channel and the uniform small Primitive-based channel, where the big Primitive structure is twice the size of the small Primitive structure. The computational domain is chosen as $\Omega = [0, 20] \times [0, 10] \times [0, 10]$. The CPU time costs for the three cases is of 33.61 s, 26.48 s, and 34.54 s, respectively. We choose the random initial condition for the phase field variable and the following initial conditions for the velocity and temperature field:

$$\phi(x, y, z, 0) = \text{rand}(x, y, z), \quad T(x, y, z, 0) = 10\psi(x, y, z), \quad \mathbf{u}(x, y, z, 0) = (10\psi(x, y, z), 0, 0). \quad (27)$$

The top row in Fig. 11 shows the velocity streamline and the bottom row shows the contour plot of the velocity field coupled with the stream slice. The quantity of streamlines indicates the fluid flow flux, and the color of the streamlines signifies the temperature value. It is important to emphasize that warmer colors correspond to higher numerical values, while cooler colors indicate lower numerical values. It is obvious that the velocity at the central slice along the x -direction is larger because of the small area. Furthermore, let us focus on the comparison results of the central slices along the y - and z -direction. As shown in Fig. 11(a), the fluid passes through central domains of the channels at a relatively large velocity, with minor change in flow velocity and direction. In contrast, the flow velocity inside the domains that do not directly connect the inlet and outlet is very small as shown in Fig. 11(c). Meanwhile, the reverse flow or the backflow can appear in these domains. Considering that the same heat fluids pass through the two channels in Fig. 11(a) and (c) with the same initial velocity, the outflow velocity of channel in (c) is smaller than that of channel (a), while the thermal conduction effect is better than that of channel (a). By combining the advantages of the two channels, we aims to design the new Primitive-based channel as shown in Fig. 11(b). As can be seen from the optimized channel, our proposed method can design and optimize continuous transition between the different scale Primitive structures and retain the main characteristics. By considering the velocity slices shown in the bottom row of Fig. 11(b), we can find that the velocity value are evenly distributed with a small measure of variation. In order to demonstrate the wellness of the new designed Primitive-based channel, we take the quantitative comparison of the relationship between pressure drop and the heat transfer coefficient and the volume share. We have shown the relationship between the pressure drop and volume share in Fig. 12(a) and the relationship between the heat transfer coefficient and volume share in Fig. 12(b). To demonstrate the conservation of volume and ensure a fair quantitative comparison, we illustrate the volumetric differences before and after optimization in Fig. 12(c). It can be observed that during the optimization process, the volume exhibits fluctuations on the order of 10^{-10} . Hence, we have a legitimate foundation to affirm the conservation of volume, rendering these quantitative comparative tests both fair and meaningful. Furthermore, the following summarizations can be obtained: (i) When $R \leq 0.5$, the composite channel composed by two sizes Primitive structures has the lower pressure drop

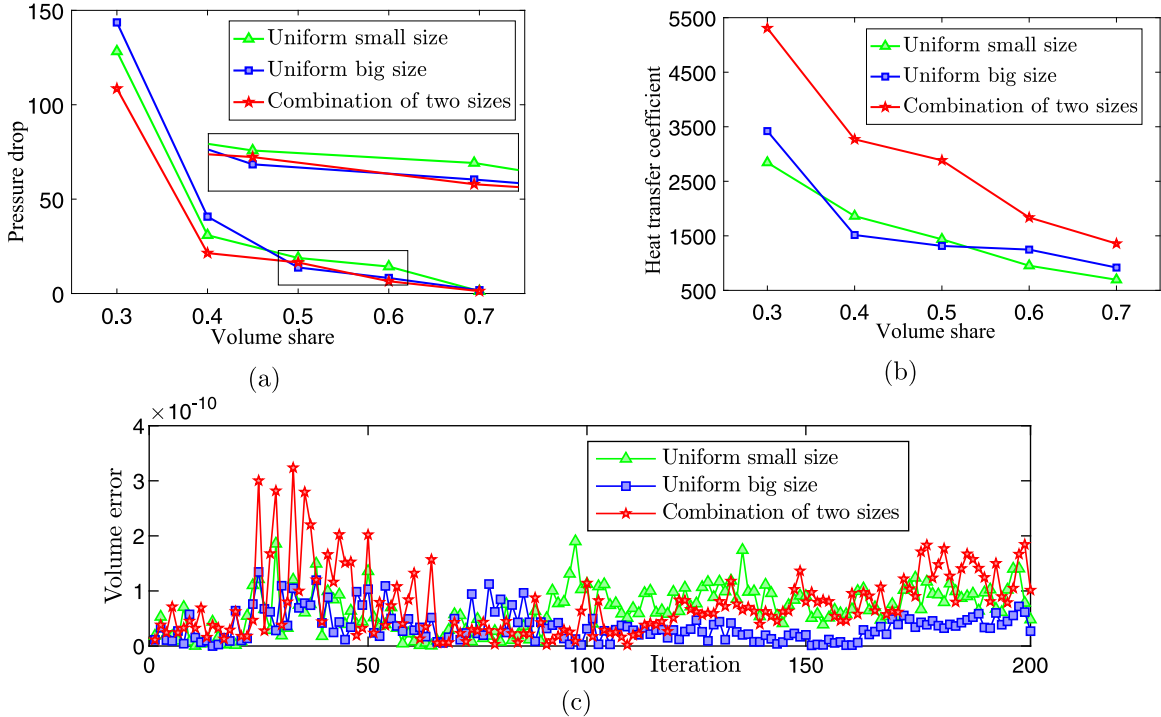


Fig. 12. Comparison results of the quantitative physical properties with the optimized channel composed of different scale Primitive structures. (a) Relationship between specific pressure drop and volume share. (b) Relationship between heat transfer coefficient and volume share. (c) The evolution results of the volume error between the optimized structure and the reference structure.

than that with the uniform Primitive structure. (ii) When $R \geq 0.6$, the pressure drop is tinyly affected by the shape of the channels, thus there are little difference between the pressure drop obtained by using the three kinds of channel. (iii) The optimized channels have larger heat transfer coefficients than the channels composed by the uniformed Primitive structures, which means that our designed channel has better thermal conductivity. Considering that the three channels only differ in the cell size of base structure, the reason that our structure conducts heat better is because it changes the direction of the flow in physical space. Inevitable changes for fluid flow direction enhances the disturbance and mixing, which contributes to the enhancement of heat transfer. In order to demonstrate that our method has a positive effect on the fluid flow, we compare the results of area-averaged velocity distribution along the flow direction as shown in Fig. 13. As can be seen from the comparison results, some summarizations should be noted: (i) The inlet and outlet velocities in our channel are consistent with the results of the uniform small Primitive channel. (ii) The flow acceleration or deceleration of the fluid flow in our channel is greater than that in the uniform channel, which is caused by the formed eight branches of the big cell structure. (iii) The large vortices have appeared at the big cell structure, which causes the significant reduction of mean velocity and keeps the low level along the direction of flow. Considering the above comparison, the optimized channel obtained by our method has demonstrated good performance in improving heat transfer capacity. In addition, the optimized structure physically reduces the pressure drop and requires less mechanical strength for the sheets of the channel.

4.8. Optimizing large-scale channels through composite structures featuring variable cell sizes of Diamond units

Inspired by the results in Table 3, which indicate that D structures perform slightly better than other structures, we attempted to use D structures for the optimization design of large-scale heat exchanger channels to demonstrate the efficiency and robustness of our algorithm. Dealing with the design of extensive heat exchanger channels involves navigating through more complex operating conditions and trade-offs between various constraints, such as heat transfer efficiency and the stress-strain distribution within the pipeline. However, such trade-offs are beyond the scope of this paper. We consider the design of TPMS-type channels for cylindrical pipes with a radius of 45 units in a computational domain of $[0, 120] \times [0, 50] \times [0, 50]$. The design includes 30 units of D structures with a size of $10 \times 10 \times 10$ and 280 units of D structures with a size of $5 \times 5 \times 5$. The composed channel is demonstrated in Fig. 14(a). To provide a clearer view of the internal structure, we have cut the pipeline in half along the x -direction to examine the connectivity of the internal components. Fig. 14(c) shows a closer view of the internal composite structure of Fig. 14(a). From the results, it can be observed that our method can be directly extensible to the optimization design of large-scale channels, which is not constrained by the size, shape, or the requisite TPMS structures. Furthermore, to illustrate the changes occurring in the optimized process of D structures, we employ three strategies for structural design within the same-sized computational domain $\Omega = [0, 20] \times [0, 10] \times [0, 10]$. The corresponding optimized results are shown in Fig. 14(d), (e), and (f), respectively. It is evident from the results that our method incorporates the coupled flow effects to ultimately achieve smooth and connected optimized channels.

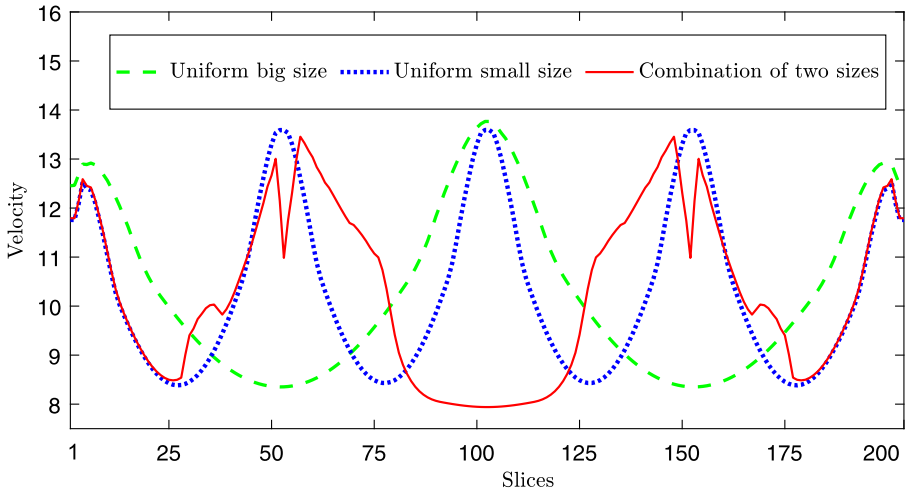


Fig. 13. Comparison results of area-averaged velocity distribution along the flow direction. The solid red line shows the results with the composite structure composed by two different sizes Primitive-based structures. The blue dotted line shows the results with the uniform small size Primitive-based structures. The green dashed line shows the results with the uniform big size Primitive-based structures.

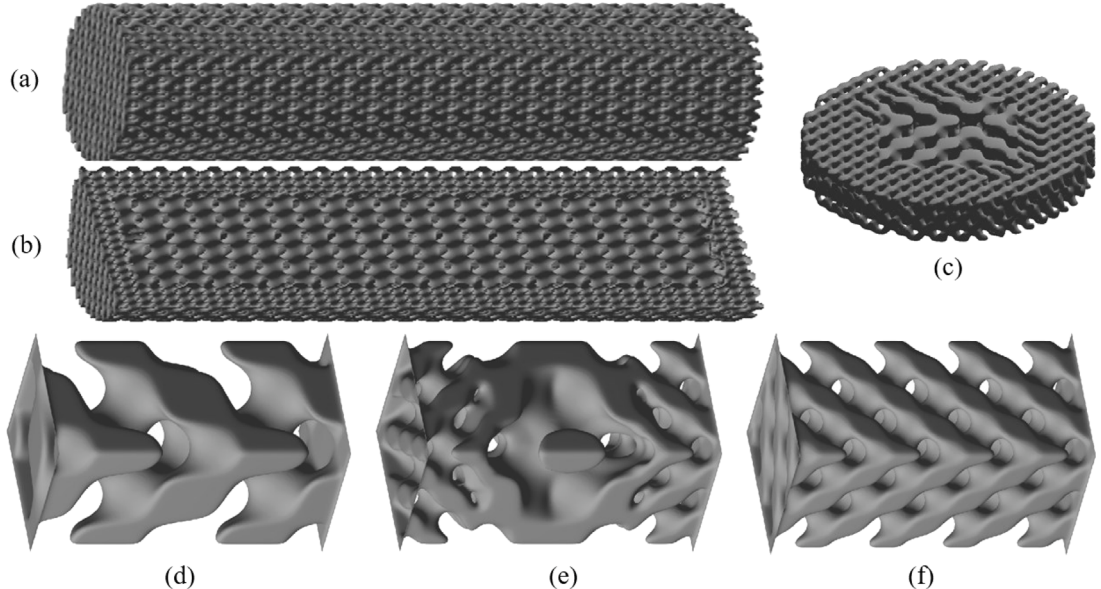


Fig. 14. Large scale channel design and comparison results of the channel composed of different scale Diamond structures. (a) Hollow cylinder composite channel with D structures. (b) Landscape closer view of (a). (c) Portrait closer view of (a). (d) The uniform big P-based channel. (e) The two-scale P-based channel. (f) The uniform small P-based channel.

5. Conclusion

In this paper, a novel TPMS based topology optimization method was proposed for the hydrodynamical and convective heat transfer, which can optimize the channels shapes to maximize the heat loss and mass flux by holding the constant mean curvature. The fluids channels with non-trivial geometries freely evolve along the optimization process with the TPMS-based assumption. We proposed a new energy functional by modifying the original energy equation based on the constant curvature property of the TPMS structure, which leads to a novel governing system composed of the Allen–Cahn type model, the Darcy–Stokes model, and the convection-diffusion heat transfer model. The Crank–Nicolson method with second order time accuracy and the central difference method with second order space accuracy were utilized to discretize the system. The Lagrange multiplier method was applied to avoid the influence of higher-order nonlinear terms and highly coupled terms on the stability of the proposed scheme. It was proved that the system satisfied the unconditional energy dissipation of the original energy in both continuous and discrete cases, which indicated that large-scale computation and large time steps can be performed. We performed various numerical

experiments and carried out topology optimization based on non-uniform TPMS structure with different porosity, types, and sizes, which demonstrated that the fluid channel with optimized structures can greatly improve heat transfer than the original TPMS-based channel from the quantitative and qualitative perspectives. What needs to be emphasized is that our investigations, involving a small number of TPMS structural units, aim to compare and individually optimize for various scenarios that may arise in the structural design of heat exchanger channels. These investigations provide convenience for large-scale channel design and adaptive design, serving as a direct extension application of the explored cases in this paper. The present work opens some relevant issues for future investigations, which can be summarized as follows:

- Our method currently specializes in the optimization of porous channels exclusively through the utilization of TPMS structures. However, its applicability is limited when adapting to channels designed with alternative structural base units.
- We have incorporated the properties of minimal surfaces into the topology optimization problem for heat conduction. The introduction of additional structural constraints, such as stiffness, stress, and flexibility, may offer new avenues for pipeline design.
- Our method, designed for heat exchanger systems, is based on convective heat transfer in porous media. However, its efficacy diminishes in application scenarios characterized by abrupt temperature variations.

CRediT authorship contribution statement

Qing Xia: Data curation, Formal analysis, Methodology, Software, Writing – original draft, Writing – review & editing. **Junxia Zhu:** Data curation, Methodology, Writing – original draft. **Qian Yu:** Formal analysis, Methodology. **Junseok Kim:** Supervision, Validation, Writing – review & editing. **Yibao Li:** Formal analysis, Methodology, Project administration, Supervision, Validation, Writing – original draft, Writing – review & editing.

Declaration of competing interest

The authors declare that they have no known competing financial interests or personal relationships that could have appeared to influence the work reported in this paper.

Data availability

No data was used for the research described in the article.

Acknowledgments

Y.B. Li is supported by National Natural Science Foundation of China (No. 12271430). Q. Xia is supported by the Fundamental Research Funds for the Central Universities, China (No. xzy022022005). The authors are grateful to the reviewers whose valuable suggestions and comments significantly improved the quality of this paper.

Appendix

Proof of Theorem 1. Let us take the derivation of the total energy with respect to time as

$$\begin{aligned} \frac{d\mathcal{J}}{dt} = & \eta(\nabla \mathbf{u}, \nabla \mathbf{u}_t) - (\mathbf{f}, \mathbf{u}_t) + (\alpha_\epsilon(\phi)\mathbf{u}, \mathbf{u}_t) + \left(\frac{\alpha'_\epsilon(\phi)}{2}|\mathbf{u}|^2, \phi_t\right) + k(T, T_t) \\ & + \left(\gamma \frac{F'(\phi)}{\epsilon^2}, \phi_t\right) + \left(\gamma \nabla \phi, \nabla \phi_t\right) + \left(\gamma \lambda \frac{g'(\phi)}{\sqrt{2\epsilon}}, \phi_t\right) - \left(\beta(\psi - \phi), \phi_t\right). \end{aligned} \quad (28)$$

By taking the L_2 inner product of Eq. (9b) with \mathbf{u}_t , we can obtain the following:

$$\begin{aligned} \left(\frac{\partial \mathbf{u}}{\partial t}, \mathbf{u}_t\right) = & -(\nabla p, \mathbf{u}_t) + (\nabla \cdot (\eta \nabla \mathbf{u}), \mathbf{u}_t) - (\alpha_\epsilon(\phi)\mathbf{u}, \mathbf{u}_t) + (\mathbf{f}, \mathbf{u}_t) \\ = & -\eta(\nabla \mathbf{u}, \nabla \mathbf{u}_t) - (\alpha_\epsilon(\phi)\mathbf{u}, \mathbf{u}_t) + (\mathbf{f}, \mathbf{u}_t), \end{aligned} \quad (29)$$

where the following identities have been applied:

$$\begin{cases} \int_{\Omega} -\nabla p \cdot \mathbf{u}_t \, dx = \int_{\Omega} p \nabla \cdot \mathbf{u}_t \, dx - \int_{\partial\Omega} p \mathbf{u}_t \cdot \mathbf{n} \, dx = - \int_{\partial\Omega} p \mathbf{u}_t \cdot \mathbf{n} \, dx = 0, \\ \int_{\Omega} \nabla \cdot (\eta \nabla \mathbf{u}) \cdot \mathbf{u}_t \, dx = - \int_{\Omega} \eta \nabla \mathbf{u} \cdot \nabla \mathbf{u}_t \, dx + \int_{\partial\Omega} \eta (\nabla \mathbf{u} \cdot \mathbf{u}_t) \cdot \mathbf{n} \, dx = - \int_{\Omega} \eta \nabla \mathbf{u} \cdot \nabla \mathbf{u}_t \, dx. \end{cases} \quad (30)$$

Let us take the L_2 inner product of Eq. (9a) with ϕ_t as follows:

$$\left(\frac{\partial \phi}{\partial t}, \phi_t\right) = -\gamma \left(\frac{F'(\phi)}{\epsilon^2}, \phi_t\right) - \gamma \left(\nabla \phi, \nabla \phi_t\right) - \gamma \left(\lambda \frac{\phi(1-\phi)}{\sqrt{2\epsilon}}, \phi_t\right) + \left(\beta(\psi - \phi) - \frac{\alpha'_\epsilon(\phi)}{2}|\mathbf{u}|^2, \phi_t\right), \quad (31)$$

by using the following identity

$$\int_{\Omega} \Delta \phi \cdot \phi_t \, dx = - \int_{\Omega} \nabla \phi \cdot \nabla \phi_t \, dx + \int_{\partial\Omega} (\nabla \phi \cdot \phi_t) \cdot \mathbf{n} \, dx = - \int_{\Omega} \nabla \phi \cdot \nabla \phi_t \, dx. \quad (32)$$

Let us take the L_2 inner product of Eq. (9d) with T as follows:

$$\left(\frac{\partial T}{\partial t}, T \right) + \left(\mathbf{u} \cdot \nabla T, T \right) = \left(\nabla \cdot (k \nabla T), T \right), \quad (33)$$

where the identity $(\mathbf{u} \cdot \nabla T, T) = 0$ has been performed due to Remark 1. By combining Eqs. (29), (31) and (33), we can obtain the dissipate energy functional as

$$\begin{aligned} \frac{d\mathcal{J}}{dt} &= \eta \left(\nabla \mathbf{u}, \nabla \mathbf{u}_t \right) - \left(\mathbf{f}, \mathbf{u}_t \right) + \left(\alpha_{\epsilon}(\phi) \mathbf{u}, \mathbf{u}_t \right) + \left(\frac{\alpha'_{\epsilon}(\phi)}{2} |\mathbf{u}|^2, \phi_t \right) + k \left(T, T_t \right) \\ &\quad + \gamma \left(\frac{F'(\phi)}{\epsilon^2}, \phi_t \right) + \gamma \left(\nabla \phi, \nabla \phi_t \right) + \gamma \left(\lambda \frac{g'(\phi)}{\sqrt{2\epsilon}}, \phi_t \right) - \left(\beta(\psi - \phi), \phi_t \right) \\ &= \left(\nabla \cdot (\eta \nabla \mathbf{u}), \mathbf{u}_t \right) - \left(\mathbf{f}, \mathbf{u}_t \right) + \left(\alpha_{\epsilon}(\phi) \mathbf{u}, \mathbf{u}_t \right) + k \left(T, T_t \right) + \left(\frac{\alpha'_{\epsilon}(\phi)}{2} |\mathbf{u}|^2, \phi_t \right) \\ &\quad + \gamma \left(\frac{F'(\phi)}{\epsilon^2}, \phi_t \right) + \gamma \left(\nabla \phi, \nabla \phi_t \right) + \gamma \left(\lambda \frac{\phi(1-\phi)}{\sqrt{2\epsilon}}, \phi_t \right) - \left(\beta(\psi - \phi), \phi_t \right) \\ &= - \left(\mathbf{u}_t, \mathbf{u}_t \right) - k^2 \left(\nabla T, \nabla T \right) - \left(\phi_t, \phi_t \right) \leq 0, \end{aligned} \quad (34)$$

which completes the proof.

Remark 1. Let us define the weak form of antisymmetric formulation of the advection term of momentum equation Eq. (9b) and the energy equation Eq. (9d) as the trilinear terms $B(\mathbf{u}, \mathbf{v}, \mathbf{w})$ and $B(\mathbf{u}, v, w)$. Then the following linear forms in the hybrid system has been performed, i.e.,

$$B(\mathbf{u}, v, w) = \frac{1}{2} \int_{\Omega} (\mathbf{u} \cdot (w \nabla v) - \mathbf{u} \cdot (v \nabla w)) \, dx, \quad (35)$$

$$B(\mathbf{u}, \mathbf{v}, \mathbf{w}) = \frac{1}{2} \int_{\Omega} ((\mathbf{u} \cdot \nabla \mathbf{v}) \mathbf{w} - (\mathbf{u} \cdot \nabla \mathbf{w}) \mathbf{v}) \, dx + \frac{1}{2} \int_{\partial\Omega} ((\mathbf{u} \cdot \mathbf{w}) (\mathbf{v} \cdot \mathbf{n}) - (\mathbf{u} \cdot \mathbf{v}) (\mathbf{w} \cdot \mathbf{n})) \, dS, \quad (36)$$

where \mathbf{n} is the normal vector which corresponds to the interface boundary S . Thus, the following identity can be obtained

$$B(\mathbf{u}, v, v) = 0, \quad \text{and} \quad B(\mathbf{u}, \mathbf{v}, \mathbf{v}) = 0, \quad (37)$$

which have been proved with details in [64]. It should be noted that these identities are not dependent with the divergence free conditions.

Proof of Theorem 2. Let us consider the difference between total discrete energies of \mathcal{J}_d^{n+1} and \mathcal{J}_d^n as follow:

$$\begin{aligned} &\mathcal{J}_d(\phi^{n+1}, \mathbf{u}^{n+1}, T^{n+1}) - \mathcal{J}_d(\phi^n, \mathbf{u}^n, T^n) \\ &= \frac{\tilde{\eta}^{n+\frac{1}{2}}}{2} \left(\|\nabla_d \mathbf{u}^{n+1}\|_d^2 - \|\nabla_d \mathbf{u}^n\|_d^2 \right) - \left(\mathbf{u}^{n+1} - \mathbf{u}^n, \mathbf{f} \right)_d + \frac{\tilde{k}^{n+\frac{1}{2}}}{2} \left(\|T^{n+1}\|_d^2 - \|T^n\|_d^2 \right) \\ &\quad + \frac{1}{2} \left(\alpha_{\epsilon}(\phi^{n+1}) |\mathbf{u}^{n+1}|^2 - \alpha_{\epsilon}(\phi^n) |\mathbf{u}^n|^2, \mathbf{1} \right) + \frac{\beta}{2} \left(\|\psi - \phi^{n+1}\|_d^2 - \|\psi - \phi^n\|_d^2 \right) \\ &\quad + \frac{\gamma}{\epsilon^2} \left(F(\phi^{n+1}) - F(\phi^n), \mathbf{1} \right)_d + \frac{\gamma}{2} \left(\|\nabla_d \phi^{n+1}\|_d^2 - \|\nabla_d \phi^n\|_d^2 \right) + \frac{\gamma \lambda}{\sqrt{2\epsilon}} \left(g(\phi^{n+1}) - g(\phi^n), \mathbf{1} \right)_d. \end{aligned} \quad (38)$$

Taking the inner product of Eq. (14a) with $-(\phi^{n+1} - \phi^n)$, we obtain

$$\begin{aligned} &- \frac{1}{\Delta t} \left(\phi^{n+1} - \phi^n, \phi^{n+1} - \phi^n \right)_d \\ &= -\gamma \left(\Delta_d \phi^{n+\frac{1}{2}}, \phi^{n+1} - \phi^n \right)_d - \beta \left(\psi - \phi^{n+\frac{1}{2}}, \phi^{n+1} - \phi^n \right)_d \\ &\quad + \left(\frac{\alpha'(\phi^n) + \alpha'(\phi^{n+1})}{4} \frac{|\mathbf{u}^n|^2 + |\mathbf{u}^{n+1}|^2}{2}, \phi^{n+1} - \phi^n \right)_d + \xi^{n+\frac{1}{2}} \left(\frac{\delta W(\tilde{\phi}^{n+\frac{1}{2}})}{\delta \phi}, \phi^{n+1} - \phi^n \right)_d \\ &= \frac{\gamma}{2} \left(\nabla_d \phi^{n+1} + \nabla_d \phi^n, \nabla_d \phi^{n+1} - \nabla_d \phi^n \right)_d + \frac{\beta}{2} \left(\|\phi^{n+1} - \psi\|_d^2 - \|\phi^n - \psi\|_d^2 \right) \\ &\quad + \left(\alpha(\phi^{n+1}) - \alpha(\phi^n), \frac{|\mathbf{u}^n|^2 + |\mathbf{u}^{n+1}|^2}{4} \right)_d + \left(W(\phi^{n+1}) - W(\phi^n), \mathbf{1} \right)_d, \end{aligned} \quad (39)$$

where the following identities have been performed:

$$\left(\frac{\alpha'(\phi^n) + \alpha'(\phi^{n+1})}{4} \frac{|\mathbf{u}^n|^2 + |\mathbf{u}^{n+1}|^2}{2}, \phi^{n+1} - \phi^n \right)_d$$

$$\begin{aligned}
&= \left(\frac{\alpha'(\phi^n) + \alpha'(\phi^{n+1})}{2} (\phi^{n+1} - \phi^n), \frac{|\mathbf{u}^n|^2 + |\mathbf{u}^{n+1}|^2}{4} \right)_d \\
&= \left(\alpha(\phi^{n+1}) - \alpha(\phi^n), \frac{|\mathbf{u}^n|^2 + |\mathbf{u}^{n+1}|^2}{4} \right)_d,
\end{aligned} \tag{40}$$

$$\begin{aligned}
-\beta(\psi - \phi^{n+\frac{1}{2}}, \phi^{n+1} - \phi^n)_d &= \frac{\beta}{2} (\phi^{n+1} + \phi^n - 2\psi, \phi^{n+1} - \phi^n)_d \\
&= \frac{\beta}{2} \|\phi^{n+1} - \psi\|_d^2 - \frac{\beta}{2} \|\phi^n - \psi\|_d^2.
\end{aligned} \tag{41}$$

Taking the inner product of Eq. (14c) with $\mathbf{u}^{n+1} - \mathbf{u}^n$, we obtain

$$\begin{aligned}
&\frac{\tilde{\eta}^{n+\frac{1}{2}}}{2} \left(\|\nabla_d \mathbf{u}^{n+1}\|_d^2 - \|\nabla_d \mathbf{u}^n\|_d^2 \right) + \frac{1}{2} \left(\alpha(\phi^{n+1}), |\mathbf{u}^{n+1}|^2 \right)_d - \frac{1}{2} \left(\alpha(\phi^n), |\mathbf{u}^n|^2 \right)_d \\
&- (\mathbf{u}^{n+1}, \mathbf{f})_d + (\mathbf{u}^n, \mathbf{f})_d \\
&= -\frac{1}{\Delta t} (\mathbf{u}^{n+1} - \mathbf{u}^n, \mathbf{u}^{n+1} - \mathbf{u}^n)_d + \frac{1}{2} (p^n + p^{n+1}, \nabla_d \cdot \mathbf{u}^{n+1} - \nabla_d \cdot \mathbf{u}^n)_d \\
&+ \frac{1}{4} \left(\alpha(\phi^{n+1}) - \alpha(\phi^n), |\mathbf{u}^{n+1}|^2 + |\mathbf{u}^n|^2 \right)_d \\
&= -\frac{1}{\Delta t} (\mathbf{u}^{n+1} - \mathbf{u}^n, \mathbf{u}^{n+1} - \mathbf{u}^n)_d + \left(\alpha(\phi^{n+1}) - \alpha(\phi^n), \frac{|\mathbf{u}^n|^2 + |\mathbf{u}^{n+1}|^2}{4} \right)_d.
\end{aligned} \tag{42}$$

Taking the inner product of Eq. (14e) with $T^{n+\frac{1}{2}}$, we obtain

$$\begin{aligned}
&\frac{1}{2\Delta t} (T^{n+1} - T^n, T^{n+1} + T^n)_d \\
&= -(\mathbf{u}^{n+\frac{1}{2}} \cdot \nabla_d T^{n+\frac{1}{2}}, T^{n+\frac{1}{2}})_d + (\nabla_d \cdot (\tilde{k}^{n+\frac{1}{2}} \nabla_d T^{n+\frac{1}{2}}), T^{n+\frac{1}{2}})_d \\
&= -\tilde{k}^{n+\frac{1}{2}} (\nabla_d T^{n+\frac{1}{2}}, \nabla_d T^{n+\frac{1}{2}})_d,
\end{aligned} \tag{43}$$

where the identity $(\mathbf{u}^{n+\frac{1}{2}} \cdot \nabla_d T^{n+\frac{1}{2}}, T^{n+\frac{1}{2}})_d = 0$ has been performed due to Remark 1. Thus, by combining Eqs. (39), (42), and (43), we obtain the energy dissipation as follows:

$$\begin{aligned}
&\mathcal{J}_d(\phi^{n+1}, \mathbf{u}^{n+1}, T^{n+1}) - \mathcal{J}_d(\phi^n, \mathbf{u}^n, T^n) \\
&= \frac{\tilde{\eta}^{n+\frac{1}{2}}}{2} \left(\|\nabla_d \mathbf{u}^{n+1}\|_d^2 - \|\nabla_d \mathbf{u}^n\|_d^2 \right) - (\mathbf{u}^{n+1} - \mathbf{u}^n, \mathbf{f})_d + \frac{\tilde{k}^{n+\frac{1}{2}}}{2} \left(\|T^{n+1}\|_d^2 - \|T^n\|_d^2 \right) \\
&+ \frac{1}{2} \left(\alpha_e(\phi^{n+1}) |\mathbf{u}^{n+1}|^2 - \alpha_e(\phi^n) |\mathbf{u}^n|^2, \mathbf{1} \right) + \frac{\beta}{2} \left(\|\psi - \phi^{n+1}\|_d^2 - \|\psi - \phi^n\|_d^2 \right) \\
&+ \frac{\gamma}{\epsilon^2} \left(F(\phi^{n+1}) - F(\phi^n), \mathbf{1} \right)_d + \frac{\gamma}{2} \left(\|\nabla_d \phi^{n+1}\|_d^2 - \|\nabla_d \phi^n\|_d^2 \right) + \frac{\gamma \lambda}{\sqrt{2\epsilon}} \left(g(\phi^{n+1}) - g(\phi^n), \mathbf{1} \right)_d \\
&= -\frac{1}{\Delta t} (\phi^{n+1} - \phi^n, \phi^{n+1} - \phi^n)_d - \left(\alpha(\phi^{n+1}) - \alpha(\phi^n), \frac{|\mathbf{u}^n|^2 + |\mathbf{u}^{n+1}|^2}{4} \right)_d \\
&- \frac{1}{\Delta t} (\mathbf{u}^{n+1} - \mathbf{u}^n, \mathbf{u}^{n+1} - \mathbf{u}^n)_d + \left(\alpha(\phi^{n+1}) - \alpha(\phi^n), \frac{|\mathbf{u}^n|^2 + |\mathbf{u}^{n+1}|^2}{4} \right)_d \\
&- \Delta t (\tilde{k}^{n+\frac{1}{2}})^2 (\nabla_d T^{n+\frac{1}{2}}, \nabla_d T^{n+\frac{1}{2}})_d \\
&= -\frac{1}{\Delta t} \|\phi^{n+1} - \phi^n\|_d^2 - \frac{1}{\Delta t} \|\mathbf{u}^{n+1} - \mathbf{u}^n\|_d^2 - \Delta t (\tilde{k}^{n+\frac{1}{2}})^2 \|\nabla_d T^{n+\frac{1}{2}}\|_d^2 \leq 0.
\end{aligned} \tag{44}$$

This completes the proof.

References

- [1] Deng H, To AC. A parametric level set method for topology optimization based on deep neural network. J Mech Eng 2021;143:091702.
- [2] Li B, Guo H, Zhuang X. Material design with topology optimization based on the neural network. Int J Comput Methods 2022;19:2142013.
- [3] Attarzadeh R, Rovira M, Duwig C. Design analysis of the Schwartz D based heat exchanger: A numerical study. Int J Heat Mass Transfer 2021;177:121415.
- [4] Wallin M, Ristinmaa M. Finite strain topology optimization based on phase-field regularization. Struct Multidiscipl Optim 2015;51:305–17.
- [5] Li Y, Wang K, Yu Q, Xia Q, Kim J. Unconditionally energy stable schemes for fluid-based topology optimization. Commun Nonlinear Sci Numer Simul 2022;111:106433.
- [6] Xia Q, Jiang X, Li Y. A modified and efficient phase field model for the biological transport network. J Comput Phys 2022;488:112192.
- [7] Lazarov B, Wang F, Sigmund O. Length scale and manufacturability in density-based topology optimization. Arch Appl Mech 2016;86:189–218.
- [8] Xia Q, Sun G, Yu Q, Kim J, Li Y. Thermal-fluid topology optimization with unconditional energy stability and second-order accuracy via phase-field model. Commun Nonlinear Sci Numer Simul 2023;116:106782.

- [9] Dilgen S, Dilgen C, Fuhrman D, Sigmund O, Lazarov B. Density based topology optimization of turbulent flow heat transfer systems. *Struct Multidiscip Optim* 2018;57:1905–18.
- [10] Yu Q, Xia Q, Li Y. A phase field-based systematic multiscale topology optimization method for porous structures design. *J Comput Phys* 2022;466:111383.
- [11] Dedé L, Borden M, Hughes T. Isogeometric analysis for topology optimization with a phase field model. *Arch Comput Methods Eng* 2012;19:427–65.
- [12] Xie W, Xia Q, Yu Q, Li Y. An effective phase field method for topology optimization without the curvature effects. *Comput Math Appl* 2023;146:200–12.
- [13] Wu C, Yang C, Xiao Q, Ke H, Xu H. Topology optimization of porous solid structures for heat transfer and flow channels in reactors with fluid-solid reaction coupling. *Int J Therm Sci* 2022;181:107771.
- [14] Soprani S, Haertel J, Lazarov B, Sigmund O, Engelbrecht K. A design approach for integrating thermoelectric devices using topology optimization. *Appl Energy* 2016;176:49–64.
- [15] Höghøj L, Nørhave D, Alexandersen J, Sigmund O, Andreasen C. Topology optimization of two fluid heat exchangers. *Int J Heat Mass Transfer* 2020;163:120543.
- [16] Borrvall T, Petersson J. Topology optimization of fluids in Stokes flow. *Internat J Numer Methods Fluids* 2003;41:77–107.
- [17] Pizzolato A, Sharma A, Maute K, Sciacovelli A, Verda V. Design of effective fins for fast PCM melting and solidification in shell-and-tube latent heat thermal energy storage through topology optimization. *Appl Energy* 2017;208:210–27.
- [18] Lee C, Jeong D, Shin J, Li Y, Kim J. A fourth-order spatial accurate and practically stable compact scheme for the Cahn–Hilliard equation. *Phys A Stat Mech Appl* 2014;409:17–28.
- [19] Asadpoure A, Guest J, Valdevit L. Incorporating fabrication cost into topology optimization of discrete structures and lattices. *Struct Multidiscip Optim* 2015;51:385–96.
- [20] Eschenauer H, olhoff N. Topology optimization of continuum structures: A review. *Appl Mech Rev* 2001;54:331–90.
- [21] Ding Y. Shape optimization of structures: a literature survey. *Comput Struct* 1986;24:985–1004.
- [22] Long K, Han D, Gu X. Concurrent topology optimization of composite macrostructure and microstructure constructed by constituent phases of distinct Poisson's ratios for maximum frequency. *Comput Mater Sci* 2017;129:194–201.
- [23] Al-Ketan O, Abu Al-Rub RK. Multifunctional mechanical metamaterials based on triply periodic minimal surface lattices. *Adv Energy Mater* 2019;21:1900524.
- [24] Al-Ketan O, Rowshan R, Al-Rub RKA. Topology-mechanical property relationship of 3D printed strut, skeletal, and sheet based periodic metallic cellular materials. *Addit Manuf* 2018;19:167–83.
- [25] Baobaid N, Ali MI, Khan KA, Al-Rub RKA. Fluid flow and heat transfer of porous TPMS architected heat sinks in free convection environment. *Case Stud Therm Eng* 2022;33:101944.
- [26] Xia Q, Sun G, Kim J, Li Y. Multi-scale modeling and simulation of additive manufacturing based on fused deposition technique. *Phys Fluids* 2023;35:034116.
- [27] Kaur I, Singh P. Flow and thermal transport characteristics of Triply-Periodic Minimal Surface (TPMS)-based gyroid and Schwarz-P cellular materials. *Numer Heat Tr A-Appl* 2021;79:553–69.
- [28] Guest J, Prévost J. Design of maximum permeability material structures. *Comput Methods Appl Mech Engrg* 2007;196:1006–17.
- [29] Li W, Yu G, Yu Z. Bioinspired heat exchangers based on triply periodic minimal surfaces for supercritical CO₂ cycles. *Appl Therm Eng* 2020;179:115686.
- [30] Iyer J, Moore T, Nguyen D, Roy P, Stolaroff J. Heat transfer and pressure drop characteristics of heat exchangers based on triply periodic minimal and periodic nodal surfaces. *Appl Therm Eng* 2022;209:118192.
- [31] Cheng Z, Xu R, Jiang PX. Morphology, flow and heat transfer in triply periodic minimal surface based porous structures. *Int J Heat Mass Transfer* 2021;170:120902.
- [32] Lee J, Oh S, Jeon E, Kim J, Park K. Functional gradation of the morphological properties of TPMS channel for enhanced flow performance. *Mater Des* 2022;224:111413.
- [33] Ozdemir M, Simsek U, Kiziltas G, Gayir C, Celik A, Sendur P. A novel design framework for generating functionally graded multi-morphology lattices via hybrid optimization and blending methods. *Addit Manuf* 2023;70:103560.
- [34] Modrek M, Viswanath A, Khan K, Ali M, Al-Rub R. An optimization case study to design additively manufacturable porous heat sinks based on triply periodic minimal surface (TPMS) lattices. *Case Stud Therm Eng* 2022;36:102161.
- [35] Strömbärg N. A new multi-scale topology optimization framework for optimal combinations of macro-layouts and local gradings of TPMS-based lattice structures. *Mech Based Des Struct* 2022;1–18.
- [36] Wang S, Jiang Y, Hu J, Fan X, Luo Z, Liu Y, et al. Efficient representation and optimization of TPMS-based porous structures for 3D heat dissipation. *Comput Aided Des* 2022;142:103123.
- [37] Modrek M, Viswanath A, Khan KA, Ali MIH, Al-Rub RKA. Multi-objective topology optimization of passive heat sinks including self-weight based on triply periodic minimal surface lattices. *Case Stud Therm Eng* 2023;42:102684.
- [38] Al-Ketan O, Ali M, Khalil M, Rowshan R, Khan K, Abu Al-Rub R. Forced convection computational fluid dynamics analysis of architected and three-dimensional printable heat sinks based on triply periodic minimal surfaces. *J Therm Sci Eng Appl* 2021;13:021010.
- [39] Ferro N, Perotto S, G M. A new fluid-based strategy for the connection of non-matching lattice materials. *Struct Multidiscip Optim* 2022;65:287.
- [40] Xia Q, Kim J, Xia B, Li Y. An unconditionally energy stable method for binary incompressible heat conductive fluids based on the phase-field model. *Comput Math Appl* 2023;123:26–39.
- [41] Li Y, Yun A, Lee D, Shin J, Jeong D, Kim J. Three-dimensional volume-conserving immersed boundary model for two-phase fluid flows. *Comput Methods Appl Mech Engrg* 2013;257:36–46.
- [42] Bendsøe M, Haber R, Jog C. A new approach to variable-topology shape design using a constraint on perimeter. *Struct Multidiscip Optim* 1996;11:1–12.
- [43] Garcke H, Hecht C, Hinze M, Kahle C. Numerical approximation of phase field based shape and topology optimization for fluids. *SIAM J Sci Comput* 2015;37:A1846–71.
- [44] Modica L. The gradient theory of phase transitions and the minimal interface criterion. *Arch Ration Mech Anal* 1987;98:123–42.
- [45] Li Y, Xia Q, Yoon S, Lee C, Lu B, Kim J. Simple and efficient volume merging method for triply periodic minimal structures. *Comput Phys Comm* 2021;264:107956.
- [46] Lee HG, Kim J. Regularized Dirac delta functions for phase field models. *Internat J Numer Methods Engrg* 2012;91:269–88.
- [47] Li Y, Guo S. Triply periodic minimal surface using a modified Allen–Cahn equation. *Appl Math Comput* 2017;295:84–94.
- [48] Chen H, Wang X. A one-domain approach for modeling and simulation of free fluid over a porous medium. *J Comput Phys* 2014;259:650–71.
- [49] Ren B, Li C, Tsubokura M. Laminar natural convection in a square cavity with 3D random roughness elements considering the compressibility of the fluid. *Int J Heat Mass Transfer* 2021;173:121248.
- [50] Alexandersen J, Aage N, Andreasen C, Sigmund O. Topology optimisation for natural convection problems. *Internat J Numer Methods Fluids* 2014;76:699–721.
- [51] Dai X, Zhang C, Zhang Y, Gulliksson M. Topology optimization of steady Navier–Stokes flow via a piecewise constant level set method. *Struct Multidiscip Optim* 2018;57:2193–203.
- [52] Cheng Q, Liu C, Shen J. A new Lagrange multiplier approach for gradient flows. *Comput Methods Appl Mech Engrg* 2020;367:113070.
- [53] Guermond J, Minev P, Shen J. An overview of projection methods for incompressible flows. *Comput Methods Appl Mech Engrg* 2006;195:6011–45.
- [54] Xia Q, Liu Y, Kim J, Li Y. Binary thermal fluids computation over arbitrary surfaces with second-order accuracy and unconditional energy stability based on phase-field model. *J Comput Appl Math* 2023;433:115319.

- [55] Shen J, Xu J, Yang J. The scalar auxiliary variable(SAV) approach for gradient flows. *J Comput Phys* 2018;353:407–16.
- [56] Li Y, Qin K, Xia Q, Kim J. A second-order unconditionally stable method for the anisotropic dendritic crystal growth model with an orientation-field. *Appl Numer Math* 2022;184:512–26.
- [57] Faulkner B, Ytreberg F. Understanding Bernoulli's principle through simulations. *Amer J Phys* 2011;79:214–6.
- [58] Kwon W, Kim J, Seo S, Shin Y. Observation of von Kármán Vortex street in an atomic superfluid gas. *Phys Rev Lett* 2016;117:245301.
- [59] Yang N, Quan Z, Zhang D, Tian Y. Multi-morphology transition hybridization CAD design of minimal surface porous structures for use in tissue engineering. *Comput Aided Des* 2014;56:11–21.
- [60] Feng J, Fu J, Shang C, Lin Z, Li B. Porous scaffold design by solid T-splines and triply periodic minimal surfaces. *Comput Methods Appl Mech Engrg* 2018;336:333–52.
- [61] Xu Z, Mendola I, Razavi N, Bagherifard S. Additive manufactured Triply Periodical Minimal Surface lattice structures with modulated hybrid topology. *Eng Struct* 2023;289:116249.
- [62] Wang J, Chen K, Zeng M, Ma T, Wang Q, Cheng Z. Investigation on flow and heat transfer in various channels based on triply periodic minimal surfaces(TPMS). *Energy Convers Manag* 2023;283:116955.
- [63] Qureshi Z, Al-Omari S, Elnajjar E, Al-Ketan O, Al-Rub R. On the effect of porosity and functional grading of 3D printable triply periodic minimal surface (TPMS) based architected lattices embedded with a phase change material. *Int J Heat Mass Transfer* 2022;183:122111.
- [64] Temam R. Sur l'approximation de la solution des équations de Navier-Stokes par la méthode des pas fractionnaires II. *Arch Ration Mech Anal* 1969;33:377–85.